JOURNAL OF PETROLOGY | VOLUME 53 | NUMBER 4 | PAGES 727–759 | 2012 | doi:10.1093/petrology/egr078

An Experimental Study of Carbonated Eclogite at 3·5–5·5 GPa—Implications for Silicate and Carbonate Metasomatism in the Cratonic Mantle

EKATERINA S. KISEEVA[1]*, GREGORY M. YAXLEY[1], JÖRG HERMANN[1], KONSTANTIN D. LITASOV[2,3], ANJA ROSENTHAL[1] AND VADIM S. KAMENETSKY[4]

[1]RESEARCH SCHOOL OF EARTH SCIENCES, THE AUSTRALIAN NATIONAL UNIVERSITY, CANBERRA, ACT 0200, AUSTRALIA

[2]DEPARTMENT OF EARTH AND PLANETARY MATERIAL SCIENCE, FACULTY OF SCIENCE, TOHOKU UNIVERSITY, SENDAI 980-8578, JAPAN

[3]V. S. SOBOLEV INSTITUTE OF GEOLOGY AND MINERALOGY, SIBERIAN BRANCH, RUSSIAN ACADEMY OF SCIENCE, NOVOSIBIRSK, 630090, RUSSIA

[4]ARC CENTRE OF EXCELLENCE IN ORE DEPOSITS AND SCHOOL OF EARTH SCIENCES, UNIVERSITY OF TASMANIA, HOBART, TAS 7001, AUSTRALIA

RECEIVED FEBRUARY 9, 2011; ACCEPTED DECEMBER 14, 2011
ADVANCE ACCESS PUBLICATION JANUARY 28, 2012

We have experimentally investigated a K-bearing altered mid-ocean ridge basalt (MORB) composition to which 10% $CaCO_3$ was added (GA1 + 10% cc), at temperatures of 1050–1400°C and pressures of 3·5–5·5 GPa. Experiments were conducted in piston-cylinder apparatus in Pt–Gr (Pt with inner graphite) and Au–Pd capsules. Sub-solidus assemblages for both sets of experiments contain clinopyroxene, garnet, carbonate, rutile, coesite and K-feldspar. Apatite was observed only in the Pt–Gr experiments. Melting behaviour in experiments using different capsule materials contrasted markedly. Experiments in Pt–Gr capsules showed the silicate solidus to be at temperatures less than 1100°C at 3·5 GPa and less than 1050°C at 4·5–5·0 GPa. These are similar (3·5 GPa) or lower (4·5–5·0 GPa) temperatures compared with the carbonate solidus (1075–1125°C at 3·5–5·0 GPa). Melts in the Pt–Gr runs evolve with increasing degree of melting from K-rich silicate melts at the lowest degree of melting to carbonate–silicate immiscible liquids and silicate–carbonate melts at intermediate degrees of melting, and finally to silicate melts at the highest degrees of melting. Experiments in Au–Pd capsules were performed only at 5·0 GPa. The carbonate solidus is between 1200 and 1225°C (at least 100°C higher than in the experiments in Pt–Gr capsules at the same pressure–temperature conditions). The first melts to be produced are carbonatitic and exhibit increasing SiO_2 content with increasing temperature. This contrast in melting behaviour is explained by the relatively rapid diffusion of H through the Pt–Gr capsules, resulting in formation of H_2O, and thus dramatically depressing both the silicate and the carbonate solidi in the Pt–Gr experiments compared with those in the Au–Pd experiments. This presumably reflects the lower permeability of Au–Pd to H, resulting in a much lower H_2O/CO_2 ratio in the Au–Pd encapsulated experiments. The presence of water in the melt was demonstrated by Fourier transform infrared (FTIR) spectroscopic analysis of one Pt–Gr experiment, indicating ~0·5 wt % H_2O in the bulk composition. Further confirmation that H_2O plays such a role in the Pt–Gr experiments was provided by an additional experiment performed in a Au–Pd capsule with ~10 wt % H_2O specifically added. In this experiment immiscible carbonate and silicate melts were observed. Carbonate–silicate liquid immiscibility is considered to occur as a result of the H_2O present in the system. These results can be applied to natural systems in several ways. First, the presence of a small amount of either silicate melt or H_2O-fluid in the system will act as a 'flux', depressing the carbonate solidus to much lower temperatures than in

*Corresponding author. Present address: Department of Earth Sciences, Oxford University, South Parks Road, Oxford OX1 3AN, UK. E-mail: kate.kiseeva@earth.ox.ac.uk

anhydrous systems. Second, the full trend in melt evolution from silicate-rich to carbonate-rich melts, which is also observed in inclusions in diamonds, can be explained by melting of K- and CO_2-bearing, water-undersaturated MORB compositions. In cratonic environments low-degree silicate and immiscible silicate and carbonate melts will metasomatize the overlying mantle in different ways, producing, in the first instance, Si enrichment and crystallization of additional orthopyroxene, phlogopite, pyrope-rich garnet and consuming olivine, and, in the second case, carbonate metasomatism, with additional magnesite–dolomite, clinopyroxene and apatite. Both metasomatic styles have been described in natural peridotite xenoliths from the cratonic lithosphere.

KEY WORDS: *experiments on MORB composition; liquid immiscibility; minor amounts of water; carbonate and silicate metasomatism; inclusions in diamonds*

INTRODUCTION

Studies of mantle xenoliths reveal the types of rocks that are common in the sub-continental lithospheric mantle. Based on the relative abundances of xenolith types in kimberlites, cratonic lithosphere is inferred to consist mainly of peridotite (both spinel and garnet facies) with a subordinate amount of pyroxenite and eclogite (Boyd *et al.*, 1997). Despite the small proportion of the eclogite component (Schulze, 1989; James *et al.*, 2004), it may participate disproportionately in melting owing to its lower solidus temperature relative to peridotite.

There are two competing hypotheses for the origin of the cratonic eclogites. The first explains them as products of high-pressure igneous fractionation in the upper mantle (Macgregor & Carter, 1970; Garlick *et al.*, 1971). The second suggests that the eclogites are the product of prograde metamorphism of subducted oceanic crust that previously underwent igneous fractionation and alteration at low pressures and low temperatures (Helmstaedt *et al.*, 1972; Schulze & Helmstaedt, 1988; Taylor & Neal, 1989; Jacob *et al.*, 1994). There are strong isotopic and compositional arguments that at least some eclogite xenoliths are remnants of oceanic crust, subducted millions of years ago and stored in the mantle (Jacob, 2004). These rocks are of particular importance for mantle heterogeneity, potentially being able to transport volatiles (CO_2, H_2O) and incompatible elements into the cratonic mantle. Hydrothermal alteration of oceanic crust introduces significant amounts of carbonate into the slab. During subduction, H_2O is efficiently removed during dehydration and melting; however, a significant part of the carbonate component is refractory in subducted mafic rocks and may be transported into the deep mantle (Molina & Poli, 2000; Kerrick & Connolly, 2001; Dasgupta & Hirschmann, 2010). Minor amounts of H_2O can still be stored in the nominally anhydrous minerals, such as clinopyroxene and garnet (Katayama & Nakashima, 2003; Katayama *et al.*, 2003), or in accessory hydrous phases such as amphibole and phlogopite. Therefore mantle eclogites may have high carbonate and low H_2O contents and these compositions should be studied experimentally.

Most previous experimental studies on carbonated eclogite systems have been conducted in the pressure–temperature (P–T) regime of subducting slabs, and used to constrain the fate of the subducted altered (carbonated) ocean floor basalt (Yaxley & Green, 1994; Hammouda, 2003; Dasgupta *et al.*, 2004, 2005; Yaxley & Brey, 2004; Gerbode & Dasgupta, 2010). The compositions used in most of these studies were simplified and usually did not contain such minor components as K, P, H_2O and Ti (Table 1). Although partial melt compositions and the solidus locations of carbonated eclogites have been experimentally determined, significant differences in solidus temperatures and shapes were attributed mainly to the influence of compositional parameters (Dasgupta *et al.*, 2004, 2005), suggesting that the bulk composition can influence the location of the solidus. In all these nominally anhydrous studies, and the water-undersaturated study by Hammouda (2003), near-solidus melts over the entire investigated pressure range were carbonatitic and not siliceous.

In this contribution, we experimentally investigate the melting behaviour of carbonate-rich altered oceanic crust under P–T conditions typical of the lithospheric mantle (3·5–5·0 GPa and 1050–1400°C). Further, we aim to investigate the influence of minor components such as K_2O and H_2O on the melting relations, the position of the solidus, and the nature and composition of the partial melts. Major emphasis is placed on the melting behaviour, occurrence and miscibility of silicate and carbonate melts in this system. The consequences of this style of melting for metasomatism of the sub-continental mantle and for the generation of a wide spectrum of magmas within the cratonic mantle and melt inclusions in diamonds are also discussed.

EXPERIMENTAL AND ANALYTICAL PROCEDURES

Starting composition and preparation

The GA1 composition used in the high-pressure experiments (Table 1) represents altered oceanic basalt (mid-ocean ridge basalt; MORB), which is somewhat elevated in alkalis compared with fresh MORB compositions (Yaxley & Green, 1994). To GA1, we added 10 wt % of calcite (cc) to broadly model average altered MORB, which contains up to 2–3 wt % CO_2 (5–6 wt % cc). In some areas (mainly the upper 500 m of the oceanic crust), altered MORB CO_2 contents may be as high as 6 wt %

Table 1: Compositions of experimental mixes from this and other experimental studies

	GA1	GA1cc	OTBC	SLEC1	EC1	GA2	LW
SiO_2	50·35	45·32	47·23	41·21	30·11	49·68	45·91
TiO_2	1·49	1·34	–	2·16	–	1·82	0·94
Al_2O_3	16·53	14·88	15·35	10·89	11·74	16·94	17·19
Cr_2O_3	–	–	–	0·09	–	0·08	–
FeO_T	9·83	8·85	8·93	12·83	10·05	9·71	7·67*
MnO	0·17	0·15	–	0·12	–	0·09	0·22
MgO	7·94	7·15	6·24	12·87	12·44	8·08	7·48
CaO	9·60	14·24	14·77	13·09	19·41	9·28	13·54
Na_2O	3·49	3·14	2·91	1·63	0·87	3·34	1·63
K_2O	0·44	0·40	0·02	0·11	–	0·37	0·14
P_2O_5	0·16	0·14	–	–	–	0·23	0·04
CO_2	0·00	4·40	4·43	5·00	15·38	–	–
H_2O	–	–	0·12	–	–	–	3·04†
Total	100·00	100·00	99·88	100·00	100·00	99·63	97·09

*Additional 2·33 wt % Fe_2O_3 was added.
†Total H_2O content is made up from 1·78 H_2O^+ and 1·26 H_2O^-.
GA1, Yaxley & Green (1994); GA1cc, GA1 + 10%cc, this study; OTBC, Hammouda (2003); SLEC1, Dasgupta *et al.* (2004); EC1, Yaxley & Brey (2004); GA2, Spandler *et al.* (2008); LW, Lambert & Wyllie (1972).

(Staudigel, 2003). In reality, calcite is probably heterogeneously distributed in the oceanic crust at various scales and any amount of carbonate in an experimental study will, to some extent, be arbitrary. The relatively high abundance of CO_2 in our experiments was intended to simplify the detection of carbonates in the run products. The GA1+10%cc composition therefore is a proxy for subducted, altered, mafic oceanic crust. It was first used by Yaxley & Green (1994), although those experiments were H_2O-saturated. Spandler *et al.* (2008) investigated the phase and melting relations of a composition (GA2) almost identical to GAl, but nominally without CO_2 or H_2O.

The starting mix was made by blending high-purity synthetic oxides of Si, Ti, Al, Mg and Mn and carbonates of Ca, Na and K. P was added as $(NH_4)_2HPO_4$. Fe was added as synthetically prepared fayalite (Fe_2SiO_4). The composition was doped with 30 trace elements with abundances of about 150 ppm, details of which will be presented elsewhere. A light green glass was created from the mixture by firing it in a graphite crucible in a N_2–air mixture at 1100°C and then quenching in water. Finally 10% of pure $CaCO_3$ was added and blended into the ground glass. Electron microprobe and laser ablation inductively coupled plasma mass spectrometry (LA-ICP-MS) analyses of fragments of the glass proved its homogeneity and established the bulk composition of the mix (Table 1). The mixture was subsequently kept in an oven at 110°C to avoid hydration.

Experimental techniques

All experiments were conducted in a 1·27 cm diameter end-loaded Boyd–England type piston-cylinder apparatus at the Research School of Earth Sciences (RSES), The Australian National University (ANU). A 200 tonne press was employed for experiments at 3·5 and 4·5 GPa, whereas for 5 and 5·5 GPa experiments an ultrahigh-pressure 500 tonne piston-cylinder press was used.

In the majority of runs, the material (10–20 mg) was encapsulated in an inner graphite capsule, which was placed in a welded outer Pt capsule. A graphite capsule was employed to avoid Fe loss by preventing contact between the mixes and the outer capsule. In some near-solidus runs, vitreous carbon spheres 80–200 μm in diameter were employed (Fig. 1c). Carbon spheres have previously proved to be a good means of segregating and trapping the melt for subsequent microprobe analysis (Pertermann & Hirschmann, 2003; Spandler *et al.*, 2008). The spheres were placed at the bottom and the top of the graphite capsules and usually did not exceed 20–30% of the total volume. Only in the run G1250 4.5 (read as GA1+10%cc at 1250°C and 4·5 GPa) was evidence of Fe loss detected both by major phase compositions and mass-balance calculations.

For several runs at 5 GPa, Au_{50}–Pd_{50} capsules with no inner graphite capsule were employed. This material was used mainly to check the effect of inner graphite on the solidus temperature. One further experiment was run at

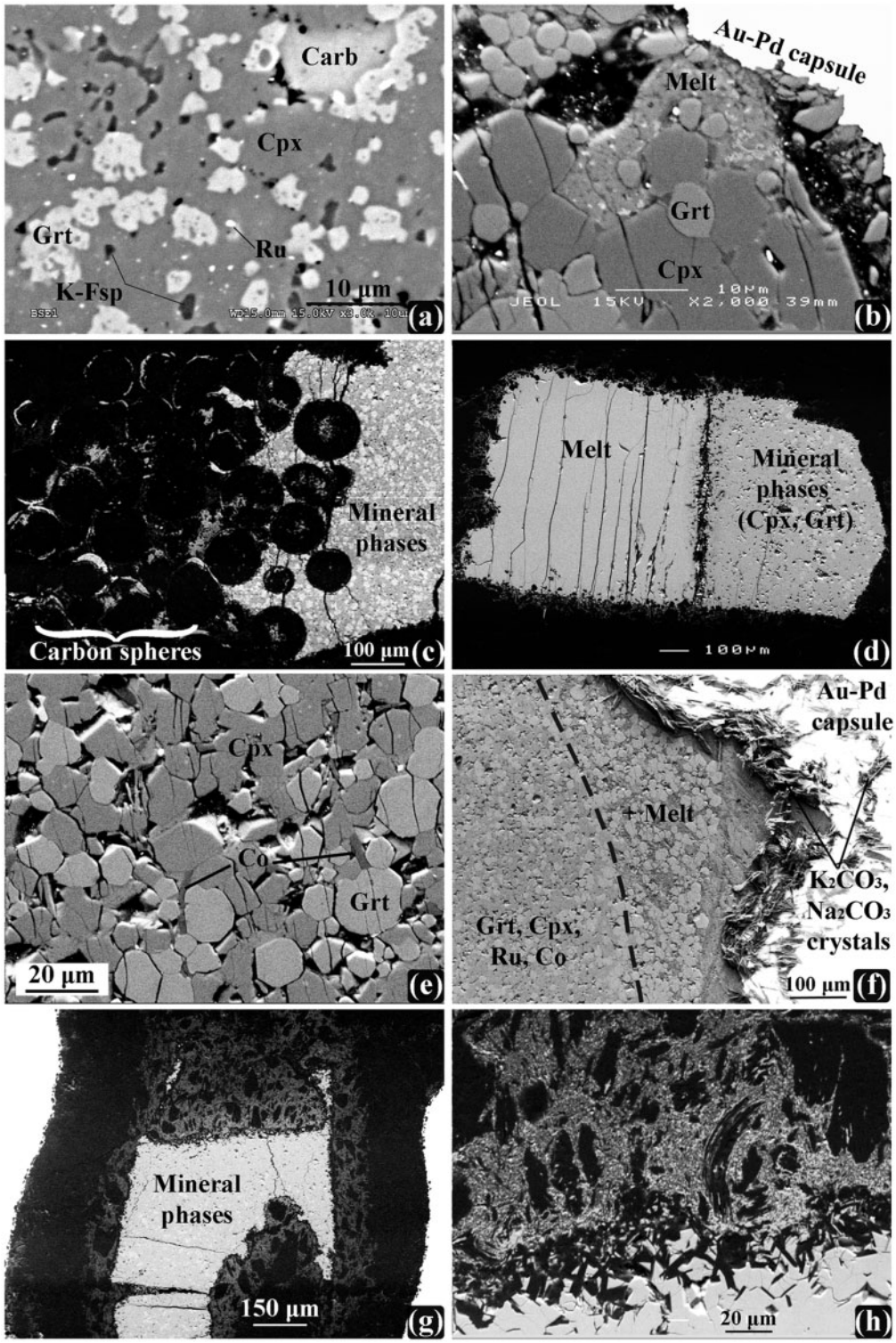

Fig. 1. BSE images of the experimental runs. (a) Run G1050.3.5. Mineral assemblage at sub-solidus conditions consisting of Grt, Cpx, Ru, Carb and K-Fsp. (b) Run G1225.5.Au–Pd. Carbonate melt with tiny quenched crystals segregated to the edge of the capsule. Bright grains are high in Ti and inferred to be small quenched rutile crystals. (c) Run G1100.5. Carbon spheres surrounded by melt. (d) Run G1350.3.5. Melt pool and mineral phases segregated to different parts of the capsule. (e) Run G1300.5.Au–Pd. Mineral assemblage consisting of Grt, Cpx, Co. (f) Run G1300.5.Au–Pd. K_2CO_3 and Na_2CO_3 fibrous crystals on the surface at the boundary between the melt pool and the Au–Pd capsule. (g) Run G1200.3.5. Silicate–carbonate melt spread throughout the capsule. Mineral phases are Grt and Cpx. (h) Enlargement of the upper part of the image area shown in (g). Abbreviations as in Table 2.

5 GPa in a Au–Pd capsule with 10 wt % free H_2O added. For this run we used a longer capsule (about 8 mm) to allow more precise measurement of the H_2O microsyringed into the capsule. The H_2O was added to test its effect on the degree of melting and the melt compositions. A standard, low-friction, salt–Pyrex, experimental assembly with graphite heaters and MgO spacers was used. All components were stored at 110°C prior to assembly and running, to avoid absorption of atmospheric water. After setting the experimental assembly in the press and programming the Eurotherm controller, the sample was heated to 600°C at a very low confining pressure (about 0·15–0·20 GPa) to soften the Pyrex. Then both pressure and temperature were increased simultaneously up to the final run conditions. No friction corrections were applied. The experiments were quenched by a rapid (less than 100°C s^{-1}) temperature decrease to room temperature by switching off the power to the furnace.

The recovered capsule was mounted in epoxy and polished in kerosene to avoid water contamination and possible dissolution of soluble carbonate materials. In some runs, the material inside the capsule was fragile and soft. In those cases it was impregnated with resin to support the fragile crystalline material so as to minimize potential loss during polishing. All of the experiments were first polished manually on abrasive paper. Then polishing machines were used with diamond pastes of 6, 3, 1·5 and 0·25 μm.

Analytical techniques; melt and mineral analysis

Run products were examined by scanning electron microscopy–energy dispersive X-ray spectroscopy (SEM-EDS) at the Centre for Advanced Microscopy, ANU. Most of the quantitative results were obtained on a JEOL 6400 scanning electron microscope fitted with an EDS detector. The accelerating voltage was 15 kV and the beam current 1 nA. Acquisition time was 120 s. Some of the analyses and back-scattered images were taken using a Hitachi 4300 field emission scanning electron microscope with an accelerating voltage of 15 kV and a beam current of 0·6 nA. A few garnet crystals were also analyzed by wavelength-dispersive spectrometry (WDS) on the Cameca SX100 electron microprobe at RSES, ANU, using a beam current of 20 nA and accelerating voltage of 15 kV. For crystalline phases, a 1 μm beam was used with about a 3–5 μm diameter excitation area. For melt analyses, if the melt formed a distinct pool, an area scan was preferred, to minimize the effects of heterogeneities on the measured compositions. Detection limits in both cases were about 0·1–0·2 wt %.

In the majority of the experiments we were able to obtain quantitative analyses of all the mineral phases observed. However, in some low-temperature runs, despite the long duration times for the experiments, mineral grains, particularly garnet, were very small (<10 μm) and contained abundant clinopyroxene inclusions, making it difficult to obtain a precise analysis. It was also not possible to analyze the tiny rutile and coesite crystals present in some runs. Although carbon spheres were used as a melt trap, precise melt compositions in runs with lower degrees of melting (<10%) were sometimes hard to obtain. In many cases, carbonate-rich melt was quenched to small patches (<5 μm) or formed thin rims around the carbon spheres. SEM-EDS analyses of the small melt patches produced low totals (sometimes lower than 50%), because during analysis of the melt the electron beam overlapped the surrounding graphite. In this case we either used the highest reliable melt totals, based on textural evidence and mass-balance calculations, and normalized the other analyses to this value, or used only elemental ratios for the trends and plots. Small melt patches were analyzed individually (spot analysis). Most quenched melts are heterogeneous, with abundant metastable quenched phases (apatite, rutile, silicates). For the experiment G1200.3.5, CO_2 concentrations in the experimental capsules were qualitatively analyzed on an Agilent 6850 gas chromatography (GC) system.

The H_2O contents in the quenched glasses in the experiment G1400.3.5 were determined by Fourier transform infrared spectrometry (FTIR) at Tohoku University, Japan. Infrared spectra were measured using a Jasco MFT-2000 microsampling FTIR spectrometer. Measurements were carried out using a tungsten light source, a Ge-coated KBr beam splitter and a high-sensitivity, wide-band MCT detector. Several hundred scans were accumulated for each spectrum with 1 cm^{-1} resolution and 100 μm apertures. Background corrections of absorbance spectra were carried out by a spline fit of the baseline defined by points outside the OH stretching region. The H_2O contents were obtained by averaging the absorbances measured on several points of the sample section. Micro-FTIR spectra were measured for double polished thin-sections of glass. The thicknesses of the thin-sections were 230–240 μm. The H_2O concentrations were determined according to the Beer–Lambert law:

$$c = \frac{18 \cdot 02 \times A}{d \times \rho} \cdot \frac{1}{\varepsilon}$$

where c is the H_2O concentration, A is the height of the OH-absorption peak at 3500 cm^{-1} above the background, d is the thickness of the specimen (in cm), ε is the extinction coefficient, which is 63 ± 31 $l\,mol^{-1}\,cm^{-1}$ for basaltic glass (Dixon *et al.*, 1995), and ρ is the density of the sample (in g l^{-1}). The same relationship is observed if integrated absorbances are substituted for peak height, giving the value of ε* of *c.* 32 000 $l\,mol^{-1}\,cm^{-2}$. The accuracy of the calculated H_2O contents is limited primarily by uncertainties in the molar absorption (extinction) coefficients.

The density of the glasses was estimated indirectly from the chemical composition in comparison with published data for basaltic glass (e.g. Stolper, 1982; Dixon *et al.*, 1995) with an additional correction for the CO_2 content based on the partial molar volume of CO_2 in carbonatite and carbonated basaltic melts (Dobson *et al.*, 1996; Ghosh *et al.*, 2007).

Approach to equilibrium and mass-balance calculations

Most runs produced well-crystallized, chemically homogeneous mineral phases, indicating reaction and an approach to equilibrium. To obtain the most representative mineral compositions about 10 grains of each phase were analyzed in every experiment.

Two thermometers based on Fe–Mg exchange between the major phases garnet and clinopyroxene were used to calculate temperatures, which were then compared with the run temperatures: those of Ellis & Green (1979) and Krogh (1988). Temperatures calculated with these thermometers are within 100°C of the nominal run temperature for all except three runs, which are within 120°C: G1100.5, G1225.5.Au–Pd and G1250.5.Au–Pd. This indicates a reasonably close approach to equilibrium for most experiments. The only run with higher temperature values estimated by the thermometers is G1250.5.Au–Pd.H_2O.

Mass-balance calculations were used for each of the experiments. For this purpose we employed the Regression in the Data Analysis tool pack in MS Excel. The regression analysis was able to balance the initial mix composition with the composition of all phases present in the run to identify the percentage of each of phase present. This least-squares approach is appropriate to balance the major elements of the experiments.

EXPERIMENTAL RESULTS

Phase relations

A summary of all run conditions and phase proportions for GA1+10%cc is given in Table 2. The observed phase assemblages were used to construct an experimental P–T phase diagram (Fig. 2).

The sub-solidus phase assemblages for both sets of experiments consist of clinopyroxene, garnet, carbonate, rutile, K-feldspar, coesite (at 4·5 and 5·0 GPa) and apatite (observed only in the Pt–Gr sub-solidus run). The textures observed in our experiments change dramatically with degree of melting. Above-solidus experiments contain quenched partial melts, which differ in the two sets of runs. In the Pt–Gr runs the partial melts can be subdivided into four types. With increasing temperature at any given pressure they are: low-degree siliceous melts, coexisting silicate and carbonate melts, silicate–carbonate melts and high-degree silicate melts. In the Au–Pd runs, the melts change from low-degree carbonatitic to siliceous at higher degrees of melting.

Nominally anhydrous experiments in a Pt–Gr capsule

Garnet is present in all the experimental runs, except those with the highest degrees of melting. The garnet grain size is typically <15–20 μm across in runs with melt present, whereas in sub-solidus and near-solidus runs it is usually <10 μm (Fig. 1a). Garnet sometimes contains multiple clinopyroxene inclusions and rarely Al-rich cores. In the 5·0 GPa runs the grains are more euhedral and have fewer inclusions than in the 3·5 and 4·5 GPa runs. At all investigated temperatures at 3·5 GPa no more than 26% garnet is present, increasing to 36% at higher pressure.

Clinopyroxene is the most abundant phase in the run products at all P–T (Fig. 1a, b and e). It is on the liquidus at 3·5 GPa, and this is consistent with experimental results obtained for anhydrous MORB-like experiments at 2–3 GPa by Pertermann & Hirschmann (2003). As with garnet, the clinopyroxene grain size increases with temperature at a given pressure, and the shape of the grains becomes more euhedral with increasing pressure (Fig. 1b and e).

Carbonate forms relatively large grains (around 10 μm) in sub-solidus and near-solidus runs (Fig. 1a), observed within the field of clinopyroxene and garnet. Rutile, coesite, K-feldspar and apatite are the accessory phases detected in the experiments. Where observed, these phases usually form tiny (1–2 μm) grains either as inclusions, or are interstitial to garnet or clinopyroxene grains. K-feldspar and apatite were detected only in the sub-solidus run at 1050°C and 3·5 GPa. At pressures ≥4·5 GPa, these minerals were no longer observed. Coesite appeared in the mineral assemblage only at pressures ≥4·5 GPa and low temperatures (1050 or 1100°C).

Melts exhibit various textures depending on their composition and the degree of melting. Low-degree siliceous melts were detected only in runs at 4·5 and 5·0 GPa at 1050–1100°C and 1050°C respectively. Such melt quenches into small patches of homogeneous glass and either occupies a small region around and within the carbon spheres or is non-uniformly distributed throughout the run material (Fig. 1c). Coexisting carbonate and silicate melts (Fig. 3a–d) were observed at all pressures at low to intermediate degrees of melting. The temperature interval of two coexisting melts expands with pressure and varies from around 50°C at 3·5 GPa to around 150°C at 5·0 GPa. This corresponds to only one run at 1100°C at 3·5 GPa, two runs (1150 and 1200°C) at 4·5 GPa and four runs (1100–1250°C) at 5·0 GPa. The only run at 5·5 GPa and 1250°C also produced two coexisting liquids. The coexisting melts either form separate pools surrounding the carbon spheres (Fig. 3a–d), or are interstitial to the residual silicate grains on the edge of the capsule at higher degrees of melting (Fig. 3f). The carbonate immiscible melt forms

Table 2: Experimental results and run conditions

Exp. no.	*T* (°C)	*P* (GPa)	*D* (h)	CM	Phases present*	L_{Carb}	L_{Si}
G1050__3.5	1050	3·5	168	Pt	Cpx [62], Grt [25], K-Fsp [3], Carb [9], Ap, Ru	0	0
G1100__3.5	1100	3·5	168	Pt	Cpx [61], Grt [26]	7	6
G1150__3.5	1150	3·5	168	Pt	Cpx [61·5], Grt [24]	0	14·5
G1200__3.5	1200	3·5	168	Pt	Cpx [55], Grt [24]	0	21
G1250__3.5	1250	3·5	120	Pt	Cpx [51], Grt [14]	0	35
G1300__3.5	1300	3·5	136	Pt	Cpx [45], Grt [10]	0	45
G1350__3.5	1350	3·5	120	Pt	Cpx [38], Grt [3]	0	59
G1400__3.5	1400	3·5	72	Pt	Cpx [20]	0	80
G1050__4.5	1050	4·5	168	Pt	Cpx [50], Grt [35], Carb [7], Co, Ru	0	7
G1100__4.5	1100	4·5	168	Pt	Cpx [55], Grt [31], Carb [6], Co, Ru	0	7
G1150__4.5	1150	4·5	168	Pt	Cpx [58·5], Grt [26], Ru	8	7
G1200__4.5	1200	4·5	168	Pt	Cpx [55], Grt [29·5]	6	9·5
G1250__4.5	1250	4·5	168	Pt	Cpx [56], Grt [24]	0	20
G1050__5	1050	5	168	Pt	Cpx [50], Grt [36·5], Carb [8], Co, Ru	0	4
G1100__5	1100	5	168	Pt	Cpx [48], Grt [36], Co [1], Ru	7·5	7·5
G1150__5	1150	5	168	Pt	Cpx [53·5], Grt [31], Ru	7·5	7·5
G1200__5	1200	5	168	Pt	Cpx [49], Grt [35]	6	10
G1250__5	1250	5	168	Pt	Cpx [51], Grt [31]	3	15
G1300__5	1300	5	96	Pt	Cpx [49], Grt [22]	0	29
G1250__5.5	1250	5·5	168	Pt	Cpx [56], Grt [27]	2	15
G1200__5__Au-Pd	1200	5	168	Au-Pd	Cpx [42], Grt [41], K-Fsp [1], Carb [9·5], Co [6], Ru	0	0
G1225__5__Au-Pd	1225	5	168	Au-Pd	Cpx [54·5], Grt [33], Co [3], Ru	9	0
G1250__5__Au-Pd	1250	5	168	Au-Pd	Cpx [45], Grt [39], Co [5], Ru	10·5	0
G1300__5__Au-Pd	1300	5	72	Au-Pd	Cpx [53], Grt [29], Co, Ru	0	17
G1250__5__H_2O†	1250	5	96	Au-Pd	Cpx [25], Grt [15]	5	55?‡

D (h), duration of the experiment in hours, CM, capsule material; Cpx, clinopyroxene; Grt, garnet; K-Fsp, K-feldspar; Carb, carbonate; Ap, apatite; Ru, rutile; Co, coesite; L_{Carb}, carbonate melt; L_S, silicate melt.
*Numbers in square brackets are wt % of the phase, extracted from mass-balance calculations. It should be noted that H_2O was excluded from these calculations. (See text for further explanation.) For phases with no wt % value included, it is considered <1 wt %.
†Run contains about 10% added H_2O. In text this run is marked as G1250__5__Au-Pd__H_2O.
‡L_{Si} was estimated visually.

irregular shapes and is usually heterogeneous and patchy compared with the sub-solidus carbonate crystals formed at lower temperatures. The proportions of carbonate and silicate melt within the heterogeneous areas can differ significantly. If we consider a random pocket composed of silicate and carbonate melt, then any of the following scenarios were observed: silicate melt > carbonate melt, carbonate melt > silicate melt (Fig. 3d), and approximately equal amounts of both melts (Fig. 3b). Carbonate exsolution from a quenched silicate melt with much dissolved carbonate should result in similar portions of silicate and carbonate. On the other hand, if two melts are present, the proportions of silicate melt and carbonate melt will vary strongly according to how much of each melt is trapped in a single cavity. With increasing temperature at the same pressure, the amount of the silicate melt pools increases. At higher temperatures (1200 and 1250°C at 5·0 GPa), it is uncertain if liquid immiscibility is present and it is not a quenching effect (Fig. 3f). Relatively large sizes of carbonate melt pools can indicate the presence of an independent carbonate melt, which has not been exsolved from the silicate melt upon quenching.

Silicate–carbonate melts were detected at intermediate degrees of melting at all pressures. They occur in two runs at 1150 and 1200°C at 3·5 GPa, in one run at 1250°C at 4·5 GPa and in one run at 1300°C and 5·0 GPa. Tiny (5 μm) isolated patches of silicate–carbonate melt tend to be spread randomly throughout the capsule (Fig. 1g and h). Our interpretation of this texture is that initially the melt contained rather high amounts of dissolved volatile

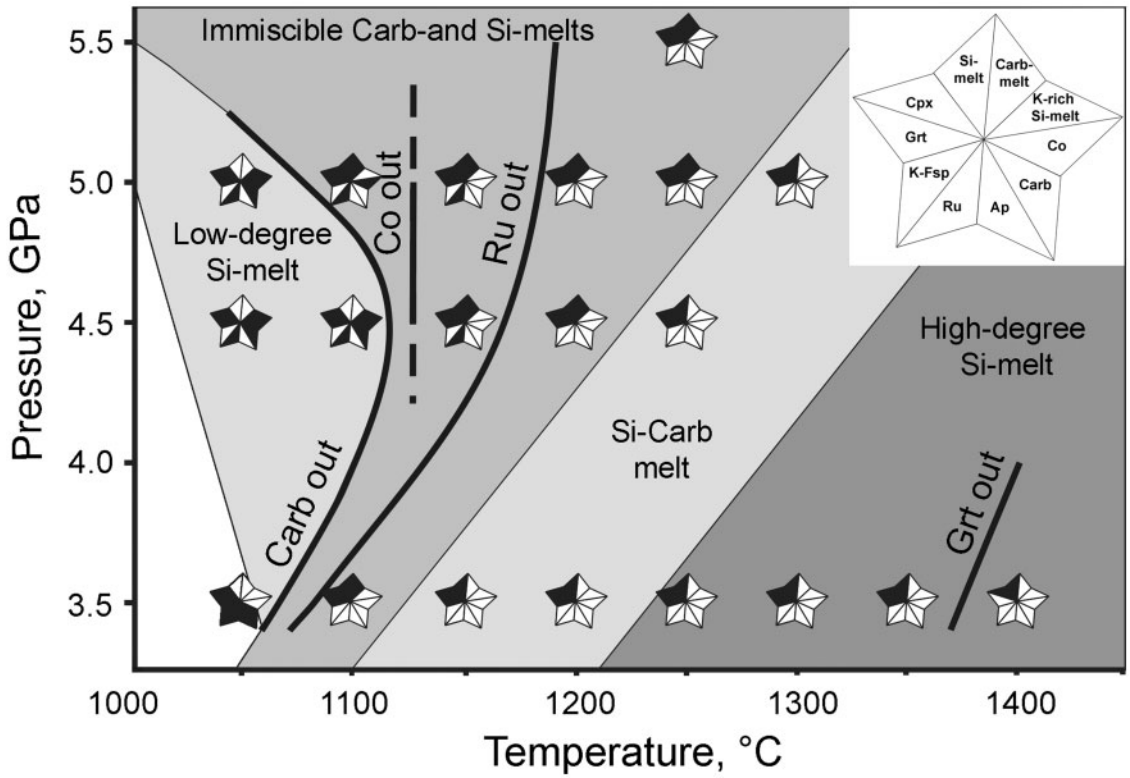

Fig. 2. Experimental *P–T* phase diagram for nominally anhydrous experiments with GA1 + 10%cc composition in Pt–Gr capsules. Abbreviations as in Table 2. Si-melt, silicate melt; Carb-melt, carbonate melt; Si-Carb melt, silicate–carbonate melt. Si-melt in the star symbol includes low-degree silicate melt, silicate–carbonate melt and high-degree silicate melt.

components, presumably mostly CO_2 or carbonate (>30–40 wt %). Upon quenching, CO_2 separated from the silicate liquid and dispersed the melt throughout significant volumes of the graphite capsule. The polishing of such runs was particularly difficult owing to the resulting vesiculation and fragmentation of the graphite capsules.

To check this hypothesis we undertook a capsule-piercing procedure, while determining the outcome using gas chromatography. The GA1+10%cc run at 1200°C and 3·5 GPa was reproduced (G1200.35). The capsule was pierced post-run under vacuum into a gas chromatograph and the spectrum revealed a CO_2 peak, consistent with the above interpretation. No H_2O peak was detected, although some H_2O may be present dissolved in the quenched melt.

We therefore infer that all the other melts that formed between the liquid immiscibility field and distinctly separated silicate melts pools produced a CO_2 fluid on quenching. Therefore compositionally we define these dispersed melts as silicate–carbonate. The definition is used because the melts contain a significant amount of both silicate and carbonate component. We must point out that decarbonation (separation of CO_2 gas on quenching) is taking place in most of the experiments, but is more pronounced in the interval corresponding to intermediate degrees of melting.

High-degree silicate melts were observed only at 3·5 GPa and temperatures higher than 1250°C. These melts quenched to separate pools of quenched glass at one end of the capsule (Fig. 1d) and are inferred to contain significant dissolved CO_2.

Nominally anhydrous experiments in a Au–Pd capsule

Five additional experiments at 5 GPa, with identical starting composition and temperatures to the 5 GPa Pt–Gr experiments, were performed in Au–Pd capsules with no inner graphite. The run at 1200°C crystallized a sub-solidus phase assemblage, with clinopyroxene, garnet, rutile, calcitic carbonate, coesite and K-feldspar. No melt was detected. At this pressure, the estimated solidus, based on the Pt–Gr encapsulated runs, is below 1050°C. Therefore an apparent 150°C increase in solidus temperature is observed in the Au–Pd encapsulated experiment relative to the Pt–Gr experiment. The first melt appeared at 1225°C and was of carbonatitic composition. This melt has a heterogeneous texture and contains quenched carbonate and other crystals (Fig. 1b). At this temperature no more solid carbonate or K-feldspar was detected, although tiny (<1 μm) K- and Al-rich patches were occasionally observed along garnet–clinopyroxene grain boundaries. The fine grain size precluded accurate

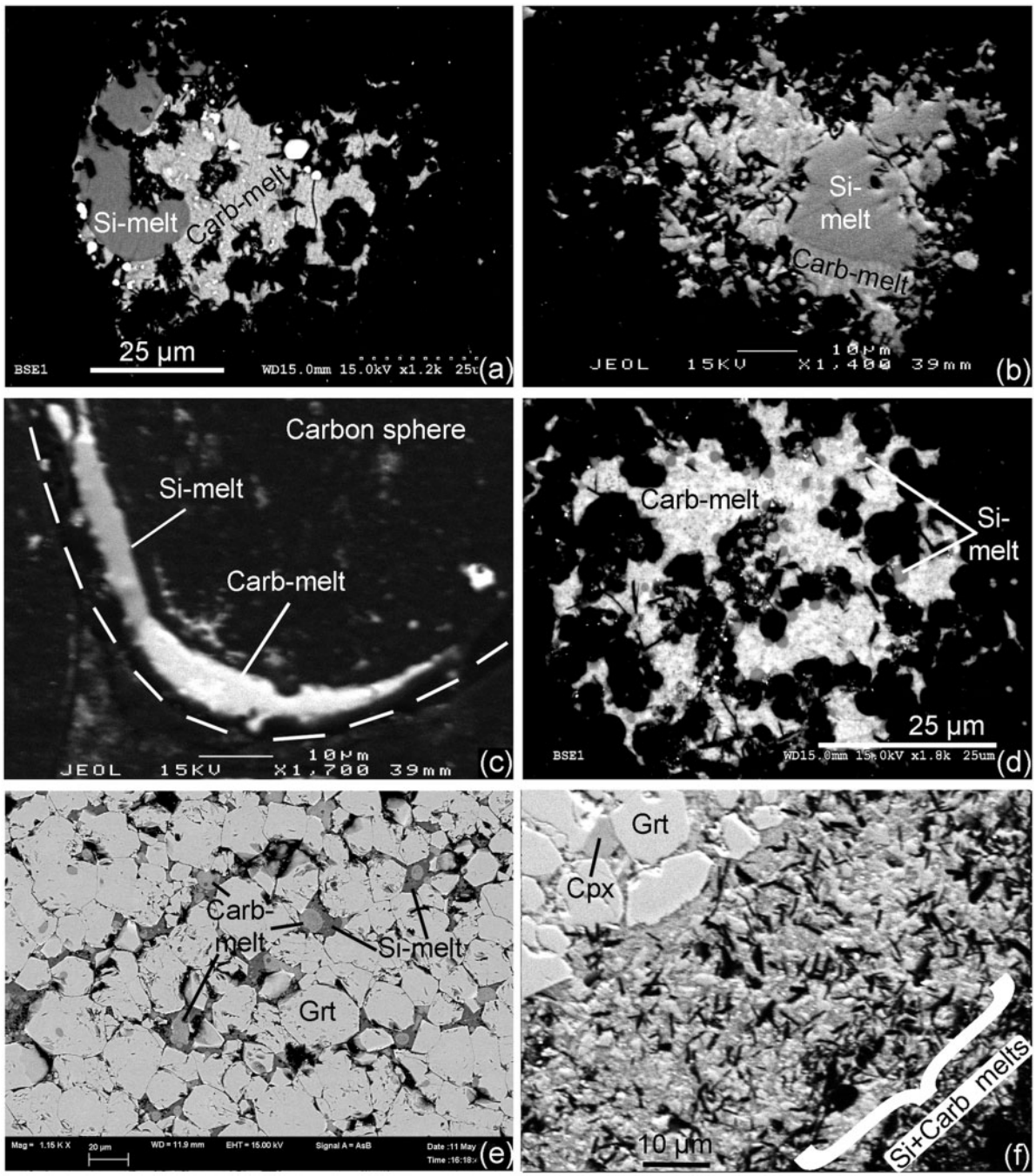

Fig. 3. BSE images of the immiscible melts (IM): silicate (dark grey) and carbonate (light grey). (a) Run G1150.45 and (b) Run G1150.5. IM within carbon sphere. Bright crystals are quenched Ru. (c) Run G1100.5. IM around the carbon sphere. (d) Run G1100.3.5. Small round ocelli of silicate melt inside a pool of carbonate melt inside a carbon sphere. (e) Run G1250.5.Au–Pd.H_2O. IM pool within crystalline grains of Grt. (f) Run G1200.5. Melt pool of (quenched) carbonate and silicate IM on the bottom of the capsule in the vicinity of Grt and Cpx. Abbreviations as in Table 2.

determination of their composition. Although we do not rule out the possibility that they are residual K-feldspar crystals, we suggest that they are more likely to be metastable K-rich phases, quenched from the K-rich carbonatitic melt. With an increase in the degree of melting, no liquid immiscibility was detected, and melts evolved towards more siliceous compositions. In G1300.5.Au–Pd a large area of quenched silicate melt was observed to have

accumulated in a pool near one of the capsule edges (Fig. 1f) with no carbonate or K-feldspar within the solid residue. Coesite persisted in all the Au–Pd runs, some of which resulted in higher degrees of melting than in the Pt–Gr experimental run at the same temperature.

Hydrous experiment in a Au–Pd capsule

One experiment was performed with the addition of free water. The run conditions were 1250°C at 5·0 GPa with about 10 wt % H_2O estimated. In this run immiscible carbonate and silicate melts were observed between garnet and clinopyroxene grains and the degree of melting was near 50% (Fig. 3e). These two melts formed rounded shapes (almost spherical) within each other. Apart from the melt present between the mineral grains, a large fraction of the melt separated at one side of the capsule. This melt was homogeneous and siliceous with a high percentage of dissolved carbonate and quenched silicate and (to a lesser extent) carbonate crystals at the capsule edges. This experiment confirms that low-degree silicate-rich melt and the coexistence of immiscible silicate-rich and carbonate-rich melts at higher degree of melting in the Pt–Gr experiments are probably explained by unavoidable contamination of the sample by the penetration of H_2O or hydrogen.

Phase compositions

In the following section we summarize the most important compositional features of the major and minor phases and experimental melts.

Garnet

Garnet compositions from all the experiments are presented in Table 3 and illustrated in Fig. 4. The grossular component of the garnets is 27–37 mol % (Fig. 4c). It usually increases slightly with pressure by 2–5 mol % from 3·5 to 4·5 GPa and remains approximately constant in all of the higher pressure runs. The garnet in Au–Pd runs is up to 3 mol % enriched in the grossular component compared with the garnet in Pt–Gr runs at the same P–T conditions.

The almandine component in garnet varies between 28 and 41 mol % (except the G1250.45 run with Fe loss, where $Grt_{alm} = 24{\cdot}6$ mol %) (Fig. 4b). It steadily decreases with temperature (i.e. degree of partial melting). For example, for the 3·5 GPa runs it decreases systematically from 41·1 at 1050°C to 31·1 mol % at 1350°C. The almandine component does not show any systematic variation with pressure. The garnet in Au–Pd is up to 2–3 mol % depleted in the almandine component.

The pyrope component in garnet varies from 27 to 41 mol % (Fig. 4a). It increases with temperature and does not display any correlation with pressure. Over the interval 1050–1150°C at all pressures, the Mg-number [molar Mg/(Mg + Fe)] of the garnet varies within the range 42–46. From 1200°C the Mg-number increases steadily to 57 at 1350°C. A significant correlation of Mg-number with pressure was not observed.

The garnet has a high TiO_2 content, which varies between 0·47 and 1·89 wt % (Fig. 4d), broadly decreasing steadily with increasing temperature. The increase in the amount of Ti in garnet at lower temperatures and its decrease at higher temperatures is inferred to relate to the presence of rutile in lower T runs and to the incompatible behaviour of Ti in garnet and clinopyroxene at temperatures above rutile-out. The amount of TiO_2 in the coexisting melts increases, complementary to its decrease in garnet (and clinopyroxene; see below). At both 4·5 and 5·0 GPa in Pt–Gr runs rutile is present at 1150°C, whereas at 3·5 GPa it was detected only in the sub-solidus run at 1050°C.

Na_2O in garnet ranges from 0·11 to 0·58 wt %. It decreases steadily with temperature at any given pressure, and tends to increase with pressure. P_2O_5 in some of the garnets reaches 0·3–0·4 wt %, but usually does not exceed 0·1–0·2 wt %.

Clinopyroxene

Clinopyroxene compositions are highly aluminous (12·29–15·75 wt % Al_2O_3) and omphacitic (Table 4, Fig. 5). At all pressures Mg-number varies between 67 and 79. At 3·5 GPa Mg-number increases throughout the melting interval from 67 at 1050°C to 77 at 1400°C. At 4·5 and 5·0 GPa in the temperature range 1050–1300°C Mg-number decreases from about 75 to 69. The amount of Na in clinopyroxene exhibits a strong positive correlation with pressure at constant temperature, but decreases with increasing temperature (Fig. 5a). At all pressures the number of Na cations per six-oxygen formula unit (p.f.u.) varies between 0·21 and 0·40. In the G1250.5.Au–Pd.H_2O run the amount of Na cations is 0·40 p.f.u., which is at least 0·5 cations p.f.u. higher than in all the other runs at the same P–T conditions.

The total amount of Al in clinopyroxene increases with increasing temperature and decreases with increasing pressure. The highest values of Al cations p.f.u. (0·64–0·67) were observed in the 3·5 GPa runs at 1300–1400°C. Al in clinopyroxenes is distributed among octahedral and tetrahedral positions. The trend for Al in the tetrahedral position (Fig. 5b) is similar to the total Al, whereas the amount of Al in octahedral coordination generally increases with pressure (following the increase of Na and hence jadeite component) and it decreases slightly with falling temperature.

The TiO_2 content of clinopyroxenes is affected by pressure, temperature and the presence or absence of rutile in the assemblage. It decreases slightly with pressure and starts decreasing with increasing temperature when rutile is no longer present as a residual phase.

Table 3: Composition of experimental garnet

	GA1 + 10%cc in Pt–Gr											
T (°C):	1050	σ	1100*	σ	1150	σ	1200	σ	1250	σ	1350†	σ
P (GPa):	3·5		3·5		3·5		3·5		3·5		3·5	
n:	3		4		6		13		15		17	
SiO_2	39·54	0·3	37·93	0·4	38·27	0·5	39·21	0·2	39·00	0·5	40·66	0·3
TiO_2	1·89	0·9	1·10	0·2	1·28	0·4	0·76	0·2	0·72	0·3	0·51	0·1
Al_2O_3	20·21	0·5	20·69	0·4	20·78	0·4	21·82	0·2	21·53	0·5	22·68	0·2
FeO	19·50	0·6	16·55	0·2	17·46	0·4	14·84	0·6	16·38	0·4	15·32	0·3
MnO	0·31	0·1	0·39	0·1	0·51	0·1	0·53	0·1	0·38	0·1	0·38	0·0
MgO	7·94	0·2	6·88	0·1	7·66	0·5	9·25	0·3	9·00	0·2	11·42	0·3
CaO	10·50	0·6	12·82	0·3	11·66	0·7	12·34	0·3	11·21	0·3	10·37	0·1
Na_2O	0·58	0·1	0·27	0·0	0·31	0·0	0·22	0·1	0·21	0·1	0·11	0·0
K_2O	b.d.l.	–	b.d.l.	–	b.d.l.	–	b.d.l.	–	b.d.l.	–	b.d.l.	–
P_2O_5	0·18	0·1	b.d.l.	–	0·14	0·1	b.d.l.	–	b.d.l.	–	0·42	0·5
Total	100·64	0·8	96·63	0·6	98·07	0·7	98·96	0·4	98·52	1·2	101·87	0·5
Mg-no.	42·06		42·56		43·86		52·62		49·46		57·04	
Components												
Grossular	28·4		36·0		32·1		33·2		30·5		26·9	
Almandine	41·1		36·3		37·5		31·1		34·7		31·1	
Pyrope	29·9		26·9		29·3		34·6		34·0		41·3	
Spessartine	0·65		0·86		1·10		1·12		0·81		0·77	

	GA1 + 10%cc in Pt–Gr											
T (°C):	1050	σ	1100	σ	1150	σ	1200	σ	1250	σ	1050	σ
P (GPa):	4·5		4·5		4·5		4·5		4·5		5	
n:	7		8		6		8		11		3	
SiO_2	39·10	0·8	39·52	0·3	38·99	0·3	39·04	0·6	40·11	0·6	38·89	0·7
TiO_2	1·52	0·3	1·03	0·3	1·05	0·4	1·11	0·2	0·92	0·2	1·23	1·0
Al_2O_3	20·70	0·3	21·35	0·5	21·20	0·3	21·31	0·8	22·00	0·4	22·21	0·5
FeO	17·59	0·9	18·35	0·4	17·37	0·1	15·96	0·4	11·90	0·4	16·47	0·3
MnO	0·34	0·0	0·39	0·1	0·38	0·1	0·41	0·1	0·47	0·1	0·32	0·1
MgO	8·20	0·3	8·09	0·2	7·33	0·1	7·89	0·3	10·33	0·3	7·16	0·2
CaO	11·41	0·8	11·66	0·5	13·21	0·2	13·04	0·2	13·69	0·3	12·53	0·3
Na_2O	0·56	0·1	0·41	0·1	0·31	0·1	0·26	0·1	0·24	0·0	0·29	0·1
K_2O	b.d.l.	–	b.d.l.	–	b.d.l.	–	b.d.l.	–	b.d.l.	–	b.d.l.	–
P_2O_5	0·33	0·1	0·24	0·1	0·15	0·1	b.d.l.	–	b.d.l.	–	0·21	0·0
Total	99·75	1·6	101·04	0·7	99·97	0·3	99·03	1·6	99·66	1·3	99·30	1·3
Mg-no.	45·40		44·00		42·90		46·84		60·72		43·64	
Components												
Grossular	31·0		31·1		35·5		35·4		36·3		35·2	
Almandine	37·3		38·2		36·4		33·9		24·6		36·1	
Pyrope	31·0		30·0		27·4		29·8		38·1		28·0	
Spessartine	0·74		0·82		0·8		0·89		0·99		0·71	

(*continued*)

Table 3: Continued

	GA1 + 10%cc in Pt–Gr											
T (°C):	1100	σ	1150	σ	1200	σ	1250	σ	1300	σ	1250	σ
P (GPa):	5		5		5		5		5		5·5	
n:	6		6		7		14		7		9	
SiO_2	38·59	0·4	39·14	0·6	39·04	0·4	39·24	0·2	39·39	0·3	39·73	0·2
TiO_2	1·76	0·3	1·50	0·5	0·70	0·2	0·77	0·2	0·87	0·2	1·07	0·2
Al_2O_3	20·49	0·1	21·32	1·0	21·28	0·3	21·52	0·2	21·58	0·3	21·46	0·2
FeO	16·83	0·6	16·18	0·5	15·85	0·1	15·75	0·4	16·08	0·4	16·48	0·2
MnO	0·49	0·1	0·32	0·1	0·33	0·1	0·32	0·1	0·34	0·1	0·34	0·0
MgO	7·59	0·2	7·73	0·3	8·18	0·1	8·28	0·2	8·43	0·1	8·15	0·1
CaO	13·12	0·5	13·17	0·6	12·72	0·2	12·99	0·3	12·54	0·1	12·66	0·2
Na_2O	0·47	0·0	0·39	0·1	0·31	0·0	0·23	0·1	0·25	0·0	0·34	0·1
K_2O	b.d.l.	–	b.d.l.	–	b.d.l.	–	b.d.l.	–	b.d.l.	–	b.d.l.	–
P_2O_5	0·20	0·1	0·12	0·1	0·11	0·1	b.d.l.	–	0·10	0·1	b.d.l.	–
Total	99·52	0·5	99·87	0·2	98·53	0·7	99·10	0·5	99·57	1·0	100·23	0·6
Mg-no.	44·55		46·00		47·92		48·38		48·30		46·83	
Components												
Grossular	35·3		35·8		34·6		35·1		33·8		34·1	
Almandine	35·3		34·3		33·7		33·2		33·8		34·7	
Pyrope	28·4		29·2		31·0		31·1		31·6		30·5	
Spessartine	1·03		0·69		0·71		0·68		0·73		0·73	

	GA1 + 10%cc in Au–Pd								H_2O	
T (°C):	1200	σ	1225	σ	1250	σ	1300	σ	1250	σ
P (GPa):	5		5		5		5		5	
n:	6		10		8		7		7	
SiO_2	38·95	0·7	39·50	0·1	40·15	0·3	39·51	0·3	39·81	0·2
TiO_2	1·18	0·3	0·86	0·2	0·89	0·1	0·86	0·1	0·47	0·1
Al_2O_3	22·51	1·5	21·06	0·2	21·56	0·2	21·13	0·2	22·24	0·1
FeO	14·42	0·3	15·26	0·3	14·22	0·3	14·75	0·4	13·54	0·4
MnO	0·36	0·1	0·39	0·1	0·39	0·1	0·41	0·1	0·35	0·1
MgO	8·56	0·2	8·11	0·2	8·60	0·1	8·65	0·3	10·44	0·3
CaO	12·16	0·7	13·71	0·2	13·84	0·2	12·97	0·1	12·21	0·1
Na_2O	0·38	0·1	0·36	0·0	0·34	0·0	0·36	0·1	0·27	0·0
K_2O	b.d.l.	–	b.d.l.	–	b.d.l.	–	0·10	0·1	b.d.l.	–
P_2O_5	0·23	0·1	0·10	0·0	b.d.l.	–	0·10	0·0	b.d.l.	–
Total	98·74	0·7	99·34	0·4	100·00	0·5	98·83	0·5	99·34	0·5
Mg-no.	51·39		48·64		51·86		51·09		57·88	
Components										
Grossular	34·1		36·9		37·2		35·2		32·5	
Almandine	31·6		32·0		29·8		31·3		28·1	
Pyrope	33·4		30·3		32·1		32·7		38·6	
Spessartine	0·79		0·83		0·84		0·87		0·74	

In this and following tables, only those analyses that were close to the theoretically correct cation sum were used. All the reported analyses are averages. b.d.l., below the detection limit (taken as 0·1 for all EDS measured values). Grossular = 100 × molar Ca/(Ca + Mg + Fe + Mn); almandine = 100 × molar Fe/(Ca + Mg + Fe + Mn); pyrope = 100 × molar Mg/(Ca + Mg + Fe + Mn); spessartine = 100 × molar (Mn/Ca + Mg + Fe + Mn).
*The measurements were made using a Hitachi FESEM.
†The measurements were made using a Cameca SX100.

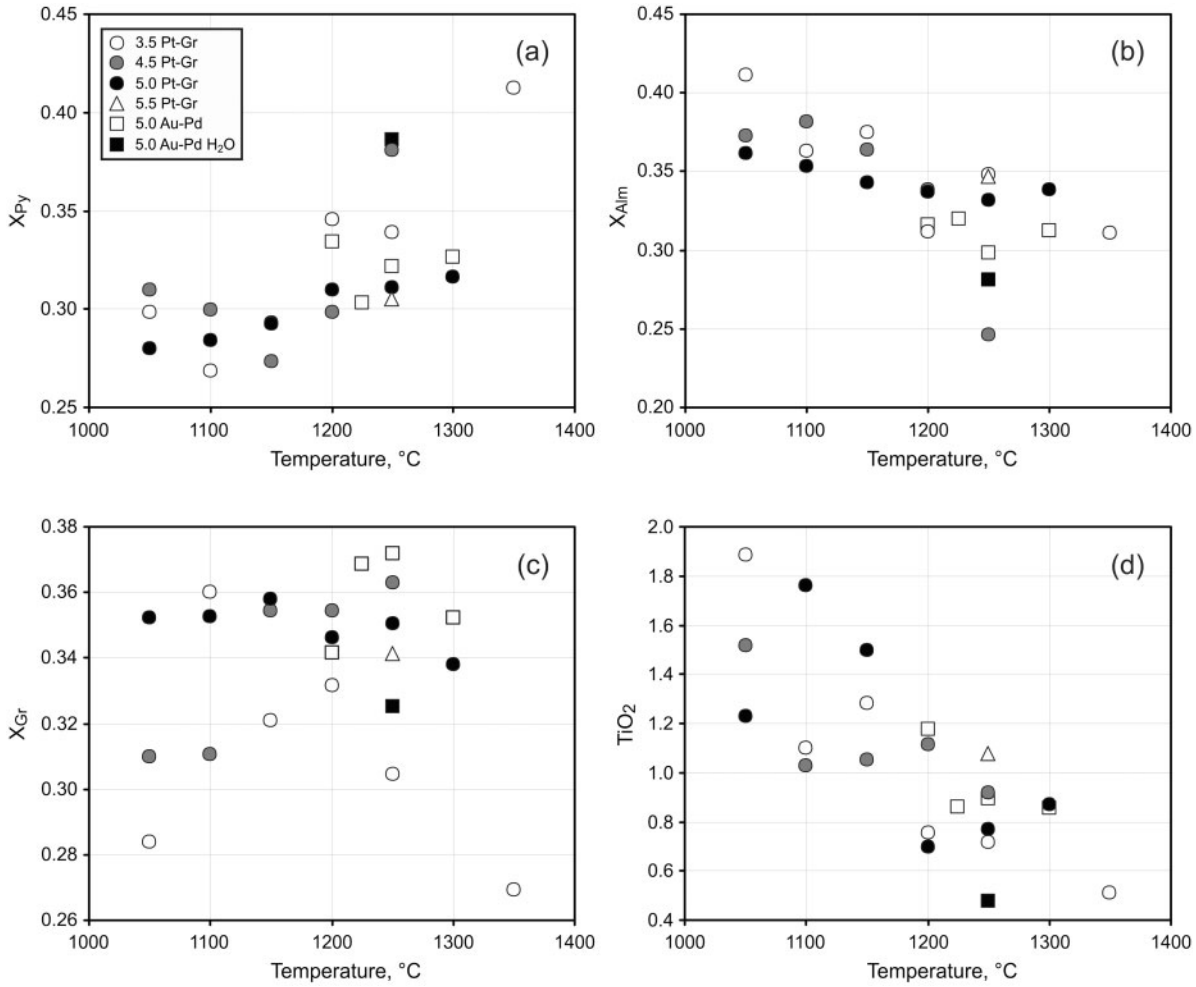

Fig. 4. Experimental Grt compositions as a function of temperature and pressure: (a) pyrope component; (b) almandine component; (c) grossular component; (d) TiO_2 in wt %. All the garnet components are molar per cent. Pt–Gr corresponds to GAl +10%cc in Pt–Gr capsule, Au–Pd corresponds to GAl +10%cc in Au–Pd capsule, Au–Pd H_2O corresponds to Au–Pd capsule with deliberately added water.

In some experiments (e.g. G1100.5), clinopyroxene crystallized in the space around the carbon spheres along with melt (Fig. 1c). This clinopyroxene is of the same composition as the clinopyroxene analyzed in the residue, although sometimes it contains slightly (up to 1%) less Fe.

Minor and accessory phases

Carbonate is represented by Mg-calcite (Table 5), which contains 82·8–92·3 mol % $CaCO_3$ with subordinate amounts of siderite (2·87–5·27 mol % $FeCO_3$) and magnesite components (4·59–11·9 mol % $MgCO_3$). These compositions are in a good agreement with those found in previous studies (Fig. 6).

K-feldspar has a sanidine composition ($(Na,K)_2AlSi_3O_8$) with up to 1·32 wt % Na_2O. Residual carbonates and K-feldspar compositions in Au–Pd runs are very similar to those reported for the Pt–Gr runs.

Although the amount of phosphorus in our starting composition is small (0·14–0·15 wt % P_2O_5), we expect a small amount of apatite to form under sub-solidus conditions, because solid carbonate together with garnet and clinopyroxene cannot incorporate all the P_2O_5 present in the system. Some of the apatite crystals are interpreted to be quenched from carbonate melt, whereas others may be present as tiny inclusions in the solid carbonate, thus contributing to the P content of the solid carbonate analysis. This can affect the SEM-EDS measurements of solid carbonates, which display relatively high P and sometimes high K values (which may be due to K-feldspar inclusions). The Mg-number of these carbonates is also relatively low.

In the 1300.5Au–Pd run, fibrous needle-like crystals of mainly K_2CO_3 (or $KHCO_3$) and rare Na_2CO_3 (or $NaHCO_3$) were observed to crystallize on the surface (Fig. 1f). Both contained a small Ca impurity. The crystals

Table 4: Compositions of experimental clinopyroxene

	GA1 + 10%cc in Pt–Gr													
T (°C):	1050	σ	1100	σ	1150	σ	1200	σ	1250	σ	1300	σ	1350	σ
P (GPa):	3·5		3·5		3·5		3·5		3·5		3·5		3·5	
n:	6		18		13		5		10		7		15	
SiO_2	51·49	0·5	50·55	1·1	50·12	0·9	49·62	0·7	49·67	0·4	49·27	0·5	49·67	0·2
TiO_2	1·42	0·3	1·23	0·4	1·42	0·1	1·02	0·1	0·84	0·1	1·14	0·2	0·56	0·0
Al_2O_3	13·83	0·7	14·09	0·6	14·01	0·8	14·59	0·4	13·86	0·4	15·75	0·3	15·29	0·3
FeO	6·70	0·3	6·04	0·2	6·49	0·3	5·44	0·2	6·66	0·3	4·41	1·0	6·48	0·2
MnO	0·12	0·1	b.d.l.	–	b.d.l.	–	b.d.l.	–	b.d.l.	–	b.d.l.	–	0·10	0·0
MgO	7·64	0·3	7·78	0·4	7·57	0·3	8·21	0·3	8·36	0·1	8·25	0·3	9·27	0·2
CaO	15·38	0·6	15·14	0·6	15·67	0·3	16·21	0·2	16·40	0·2	16·49	0·3	16·83	0·1
Na_2O	4·64	0·2	4·67	0·2	4·27	0·1	3·73	0·0	3·68	0·1	3·62	0·2	3·28	0·1
K_2O	b.d.l.	–	b.d.l.	–	b.d.l.	–	b.d.l.	–	b.d.l.	–	b.d.l.	–	b.d.l.	–
P_2O_5	b.d.l.	–	b.d.l.	–	b.d.l.	–	b.d.l.	–	b.d.l.	–	b.d.l.	–	b.d.l.	–
Total	101·21	0·3	99·50	2·0	99·55	1·4	98·83	1·2	99·47	0·4	98·93	0·7	101·49	0·7
Atoms per 6-oxygen formula unit														
Si	1·84		1·83		1·82		1·81		1·81		1·79		1·76	
Ti	0·04		0·03		0·04		0·03		0·02		0·03		0·02	
Al	0·58		0·60		0·60		0·63		0·60		0·67		0·64	
Fe	0·20		0·18		0·20		0·17		0·20		0·13		0·19	
Mn	0·00		–		–		–		–		–		0·00	
Mg	0·41		0·42		0·41		0·45		0·45		0·45		0·49	
Ca	0·59		0·59		0·61		0·63		0·64		0·64		0·64	
Na	0·32		0·33		0·30		0·26		0·26		0·25		0·23	
K	–		–		–		–		–		–		–	
P	–		–		–		–		–		–		–	
∑Cation	3·98		3·99		3·98		3·98		3·99		3·97		3·98	
Mg-no.	67·00	1·5	69·65	0·9	67·51	1·3	72·89	0·5	69·14	0·8	77·05	1·3	71·82	0·8

(*continued*)

were observed during the microprobe analysis 3 weeks after the capsule was polished and carbon coated.

Melt composition of the experiments in a Pt–Gr capsule

Representative melt compositions are presented in Table 6 and plotted in Fig. 7. The SiO_2 content of the silicate melts in this study (Fig. 7d) varies over a wide range from >60 wt % near the solidus decreasing to <40 wt % at higher degrees of melting. Although sample parts and starting materials were carefully dried prior to experiments, the presence of low-degree silica-rich melt may indicate contamination of the samples by H_2O during the experiments. It is difficult to determine the H_2O content of low-degree partial melts. However, it was possible to determine them in the high-temperature runs, where large sections of silica-rich glass were present (Fig. 1d). The H_2O contents were determined in sample G1400.3.5 as 0·87 wt % (Fig. 8). Extrapolation of these values to the total H_2O content in the samples may indicate up to 0·5 wt % H_2O after the run. Accordingly, the low-degree SiO_2-rich partial melts may contain up to 5–7 wt % H_2O.

At very low degrees of melting (<7%) in the 4·5 and 5·0 GPa runs siliceous melts in equilibrium with solid carbonate, garnet, clinopyroxene, rutile and coesite were formed. Because of their high K content (Fig. 7b) and compositional similarity to K-feldspar, they could be mistaken for K-feldspar grains. However, they also display low totals (about 80–90%) owing to the presence of a small amount of dissolved volatiles and the cation sums are inconsistent with a feldspar structure, which led to their interpretation as melts rather than K-feldspar crystals. Also, low-degree Si melts contain measurable

Table 4: Continued

	GA1 + 10%cc in Pt-Gr													
T (°C):	1400	σ	1050	σ	1100	σ	1150	σ	1200	σ	1250	σ	1050	σ
P (GPa):	3·5		4·5		4·5		4·5		4·5		4·5		5	
n:	8		8		9		7		11		6		6	
SiO_2	49·79	0·2	53·60	0·8	54·15	0·5	52·56	0·2	52·25	0·5	52·01	0·3	54·58	0·6
TiO_2	0·51	0·2	0·76	0·3	0·98	0·5	1·03	0·1	1·06	0·1	0·87	0·1	0·90	0·4
Al_2O_3	15·54	0·4	12·81	0·3	13·47	0·7	13·05	0·5	13·65	0·5	15·35	1·0	12·56	0·5
FeO	5·38	0·6	4·59	0·2	5·59	0·3	5·96	0·1	5·87	0·3	3·87	0·7	4·47	0·2
MnO	b.d.l.	–	b.d.l.	–	b.d.l.	–	b.d.l.	–	b.d.l.	–	0·16	0·1	b.d.l.	–
MgO	10·18	0·2	7·74	0·2	7·58	0·3	7·56	0·2	7·63	0·2	8·22	0·2	7·55	0·2
CaO	16·56	0·6	13·57	0·3	13·82	0·4	14·83	0·3	14·73	0·4	15·51	0·4	13·32	0·5
Na_2O	3·00	0·1	5·54	0·1	5·45	0·2	4·77	0·1	4·56	0·2	4·32	0·1	5·79	0·3
K_2O	b.d.l.	–	b.d.l.	–	b.d.l.	–	b.d.l.	–	b.d.l.	–	b.d.l.	–	b.d.l.	–
P_2O_5	b.d.l.	–	b.d.l.	–	b.d.l.	–	b.d.l.	–	b.d.l.	–	b.d.l.	–	b.d.l.	–
Total	100·96	0·4	98·62	1·6	101·14	0·6	99·74	0·4	99·74	0·7	100·31	0·6	99·17	1·0
Atoms per 6-oxygen formula unit														
Si	1·78		1·93		1·93		1·89		1·88		1·85		1·95	
Ti	0·01		0·02		0·02		0·03		0·03		0·02		0·02	
Al	0·65		0·54		0·54		0·55		0·58		0·64		0·53	
Fe	0·16		0·14		0·14		0·18		0·18		0·12		0·13	
Mn	–		–		–		–		–		0·00		–	
Mg	0·54		0·42		0·42		0·41		0·41		0·44		0·40	
Ca	0·63		0·52		0·52		0·57		0·57		0·59		0·51	
Na	0·21		0·39		0·39		0·33		0·32		0·30		0·40	
K	–		–		–		–		–		–		–	
P	–		–		–		–		–		–		–	
∑Cation	3·98		3·96		3·97		3·96		3·96		3·95		3·95	
Mg-no.	77·15	1·59	75·05	0·9	70·72	1·72	69·34	0·79	69·88	1·52	79·19	2·85	75·06	0·75

(*continued*)

TiO_2, and other components, usually not present in K-feldspar. We therefore infer that they were melts at run conditions, which quenched to glasses. The low totals are considered to be a result of significant CO_2 (Fig. 7a) and H_2O dissolved in these melts.

The two coexisting melts, present at temperatures above the low-degree alkali-rich siliceous melting field, always exhibit carbonate and silicate compositions. Carbonate melts in all the runs appear only when coexisting with immiscible silicate melt. Although the carbonate melts seem to be similar in composition to solid carbonates, they can be clearly distinguished from them. First, the melts have much lower Mg-number and lower Ca-number (Fig. 6). Also, the addition of minor elements is very useful for the distinction, as the carbonate melts have high Ti, P and K contents (up to 3·98 wt % TiO_2, 1·46 wt % Na_2O, 3·30 wt % P_2O_5 and 3·00 wt % K_2O), whereas in the sub-solidus carbonates these element concentrations are much lower (often below detection limits).

The SEM-EDS totals of the carbonate immiscible melts are very low (about 55–65%), because of the large amount of carbonate component. In some cases, small grains of quenched apatite are present within the melt. All calcitic carbonate melts have fairly high Fe and Mg contents (5·83–9·72 wt % FeO and 3·02–4·73 wt % MgO). SiO_2 contents can vary within a wide range (from 0·59 to 17·5 wt % SiO_2) and tend to increase with increasing temperature. At higher temperatures the carbonate and silicate melt compositions approach each other and the proportion of silicate melt increases.

The silicate melts display significantly higher microprobe totals (75–90 wt %) than the coexisting carbonate-rich melts. These melts are usually K-rich (2·67–10·2 wt % K_2O) (Fig. 7b) and resemble the compositions of

Table 4: Continued

	GA1 + 10%cc in Pt-Gr												Au-Pd	
T (°C):	1100	σ	1150	σ	1200	σ	1250	σ	1300	σ	1250	σ	1200	σ
P (GPa):	5		5		5		5		5		5·5		5	
n:	8		6		6		11		10		10		6	
SiO_2	54·57	0·5	53·80	0·2	53·37	0·3	52·79	0·2	52·06	0·4	54·05	0·4	53·84	0·9
TiO_2	0·57	0·1	0·80	0·1	0·63	0·0	0·74	0·1	0·86	0·1	0·92	0·1	0·68	0·1
Al_2O_3	12·29	0·4	13·25	0·3	13·12	0·2	13·27	0·2	13·73	0·3	13·68	0·3	13·71	0·5
FeO	4·58	0·2	5·40	0·2	4·90	0·1	5·32	0·1	6·25	0·2	5·61	0·3	4·79	0·2
MnO	b.d.l.	–	b.d.l.	–	b.d.l.	–	b.d.l.	–	b.d.l.	–	b.d.l.	–	b.d.l.	–
MgO	8·41	0·2	7·65	0·1	7·77	0·1	7·55	0·1	7·72	0·1	7·62	0·1	7·13	0·2
CaO	14·85	0·3	14·45	0·2	13·66	0·2	14·19	0·2	14·67	0·2	14·05	0·3	12·93	0·6
Na_2O	5·12	0·1	4·90	0·1	5·24	0·0	5·00	0·1	4·58	0·1	4·92	0·2	5·34	0·2
K_2O	b.d.l.	–	b.d.l.	–	b.d.l.	–	b.d.l.	–	b.d.l.	–	b.d.l.	–	0·20	0·1
P_2O_5	b.d.l.	–	b.d.l.	–	b.d.l.	–	b.d.l.	–	b.d.l.	–	b.d.l.	–	0·14	0·1
Total	100·38	0·5	100·25	0·3	98·68	0·7	98·85	0·4	99·86	0·6	100·83	0·4	98·75	0·7
Atoms per 6-oxygen formula unit														
Si	1·94		1·91		1·92		1·91		1·87		1·91		1·93	
Ti	0·02		0·02		0·02		0·02		0·02		0·02		0·02	
Al	0·51		0·56		0·56		0·57		0·58		0·57		0·58	
Fe	0·14		0·16		0·15		0·16		0·19		0·17		0·14	
Mn	–		–		–		–		–		–		–	
Mg	0·44		0·41		0·42		0·41		0·41		0·40		0·38	
Ca	0·56		0·55		0·53		0·55		0·57		0·53		0·50	
Na	0·35		0·34		0·37		0·35		0·32		0·34		0·37	
K	–		–		–		–		–		–		0·01	
P	–		–		–		–		–		–		0·00	
∑Cation	3·96		3·95		3·96		3·96		3·97		3·94		3·93	
Mg-no.	76·61	0·7	71·61	0·7	73·85	0·4	71·66	0·5	68·74	0·6	70·77	1·0	72·61	0·9

(*continued*)

the low-degree siliceous melts. However, with increasing temperature, the silicate melts become less potassic and more magnesian and calcic. TiO_2 (Fig. 7c) varies from 1·26 to 4·32 wt %. The Fe and Mg contents of these melts are lower than in the coexisting carbonate melts, whereas Na_2O is higher. Summarizing the compositions of coexisting carbonate and silicate melts: K, Al and to a lesser extent Na tend to be concentrated in the silicate melts, whereas P, Mg, Fe and Ca are incorporated into the carbonate melt. Mn partitions into garnet and is present in all the melts in very low abundances. Eventually the abundances of all the components in the melts converge and the textural evidence of immiscibility disappears.

It is important to note that the solid residue coexisting with the two immiscible melts does not change markedly with increasing temperature. When the immiscibility gap is wide, both rutile and coesite are present as crystalline phases. With increasing temperature, they contribute to the silicate (coesite, rutile) and carbonate (rutile) melts, increasing the proportion of the immiscible silicate melt. Melting of some additional clinopyroxene and garnet also contributes to the increasing proportion of silicate melt.

As mentioned above, because of the high CO_2 content some of the melts undergo decarbonation on quenching and form dispersed textures. Compositionally these melts can be slightly different. Their field covers that of the silicate–carbonate melts, which are difficult to analyze. The patches they create within the capsule consist of dispersed quenched material, which is often smaller than 1–2 μm. However, after normalizing the totals to the highest value, the melts display consistent compositions with 37·1–42·0 wt % SiO_2. The melts are Al-rich (9·0–12·9 wt % Al_2O_3) and contain 9·4–15·9 wt % CaO. The amount

Table 4: Continued

	GA1 + 10%cc in Au–Pd						H_2O	
T (°C):	1225	σ	1250	σ	1300	σ	1250	σ
P (GPa):	5		5		5		5	
n:	10		7		11		7	
SiO_2	53·10	0·2	53·88	0·4	52·57	0·6	53·39	0·3
TiO_2	0·92	0·1	0·94	0·2	0·67	0·2	0·36	0·1
Al_2O_3	13·67	0·2	13·93	0·2	13·65	0·3	14·08	0·2
FeO	5·95	0·2	5·50	0·2	5·62	0·3	5·41	0·3
MnO	b.d.l.	–	b.d.l.	–	b.d.l.	–	b.d.l.	–
MgO	7·15	0·1	7·39	0·1	7·16	0·1	7·32	0·3
CaO	14·09	0·1	14·11	0·1	13·57	0·2	13·00	0·3
Na_2O	4·82	0·1	4·83	0·1	4·95	0·1	5·78	0·1
K_2O	b.d.l.	–	0·14	0·1	b.d.l.	–	b.d.l.	–
P_2O_5	b.d.l.	–	b.d.l.	–	b.d.l.	–	b.d.l.	–
Total	99·69	0·5	100·73	0·5	98·19	1·2	99·34	0·5
Atoms per 6-oxygen formula unit								
Si	1·90		1·91		1·91		1·91	
Ti	0·02		0·03		0·02		0·01	
Al	0·58		0·58		0·58		0·60	
Fe	0·18		0·16		0·17		0·16	
Mn	–		–		–		–	
Mg	0·38		0·39		0·39		0·39	
Ca	0·54		0·54		0·53		0·50	
Na	0·34		0·33		0·35		0·40	
K	–		–		–		–	
P	–		–		–		–	
∑Cation	3·94		3·93		3·95		3·97	
Mg-no.	68·18	0·4	70·53	0·6	69·41	1·0	70·69	1·8

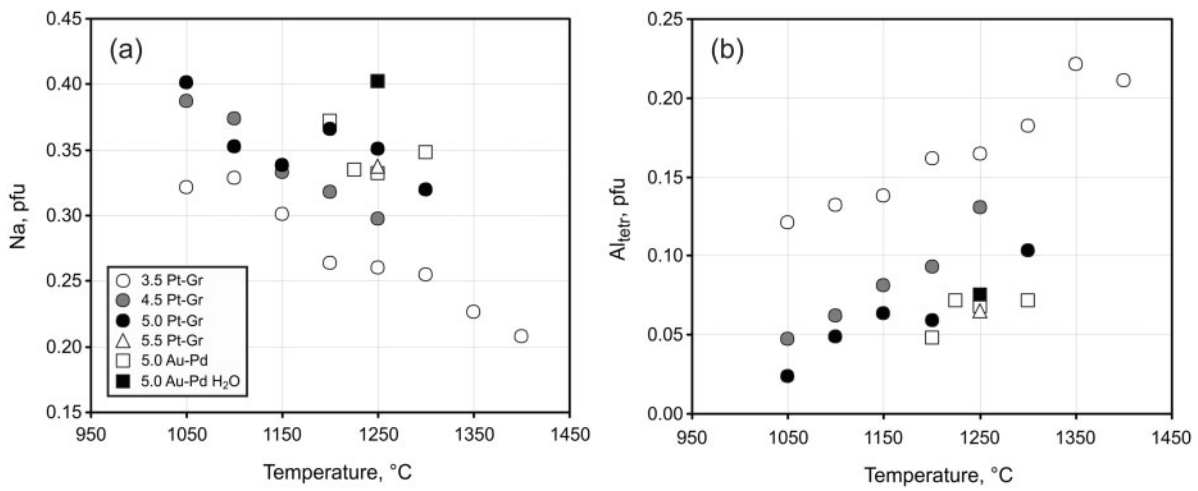

Fig. 5. Experimental Cpx compositions as a function of temperature and pressure. (a) Na content; (b) Al in tetrahedral coordination. (See Fig. 4 for legend explanations.)

Table 5: Compositions of experimental carbonate and K-feldspar

Mineral:	Carb	Carb	Carb	Carb	Carb	Fspar	Fspar
Capsule:	Pt–Gr	Pt–Gr	Pt–Gr	Pt–Gr	Au–Pd	Pt–Gr	Au–Pd
T (°C):	1050	1050	1100	1050	1200	1050	1200
P (GPa):	3·5	4·5	4·5	5	5	3·5	5
SiO_2	0·73	b.d.l.	b.d.l.	0·24	0·30	62·79	62·62
TiO_2	b.d.l.	b.d.l.	b.d.l.	b.d.l.	b.d.l.	0·19	b.d.l.
Al_2O_3	0·2	0·08	0·13	0·14	0·26	17·65	16·91
FeO	2·02	2·73	2·80	3·55	1·92	0·22	0·96
MnO	b.d.l.	b.d.l.	b.d.l.	0·11	b.d.l.	b.d.l.	b.d.l.
MgO	1·69	3·87	2·63	4·50	2·73	b.d.l.	1·67
CaO	47·32	45·97	47·27	43·55	46·86	b.d.l.	2·86
Na_2O	0·17	b.d.l.	b.d.l.	b.d.l.	0·10	0·78	1·32
K_2O	0·16	0·21	0·25	0·19	0·63	14·90	12·27
P_2O_5	1·02	0·49	0·65	0·34	0·62	b.d.l.	0·18
CO_2	46·69	46·64	46·27	47·39	46·59	–	–
Total	100·00	100·00	100·00	100·00	100·00	96·72	98·87
Mg-no.	59·85	71·59	62·50	69·24	68·83	–	–
Atoms per 8-oxygen formula unit							
Si						2·99	2·93
Ti						0·01	–
Al						0·99	0·93
Fe						0·01	0·04
Mn						–	–
Mg						–	0·12
Ca						0·00	0·14
Na						0·07	0·12
K						0·91	0·73
P						0·00	0·01
Total						4·99	5·02

The amount of CO_2 in carbonate is estimated from the EDS totals.

of incompatible elements such as K and P tends to decrease with increasing temperature.

From around 35% up to complete melting, the melts become more siliceous (42·2–45·3 wt % SiO_2) and are referred to as high-degree silicate melts. The amount of inferred dissolved CO_2 decreases (<12%, based on mass-balance calculations and the EDS analysis totals). The composition of these melts is similar to the very small interstitial quenched melt pools, analyzed between grains in these experiments, and hence equilibrium was reached.

Melt composition of the experiments in a Au–Pd capsule

A low-degree carbonate melt was observed in the G1225.5.Au–Pd run (Fig. 1b). Although the melt occupies areas at the boundary between the capsule and the run material, it was not possible to precisely determine its composition owing to the many garnet, clinopyroxene, rutile and other phases included in the melt patches. Broadly it is calcio-dolomitic with a high P content (2·4 wt % P_2O_5) and 1·18 wt % K_2O. Because no residual K-rich phase was detected in this run, this suggests a deficit in the K mass balance, and that the true melt composition was significantly more potassic. Intermediate silicate–carbonate melt observed in the G1300.5.Au–Pd run is very low in SiO_2 (35·7 wt %) and includes a high amount of CO_2 (about 25 wt %), TiO_2 (3·17 wt %), and K_2O (3·60 wt %).

There are three distinct melts in the G1250.5.Au–Pd.H_2O run: carbonate and silicate immiscible melts, which occur between the mineral phases, and a high-degree silicate melt, which occupies about half of the

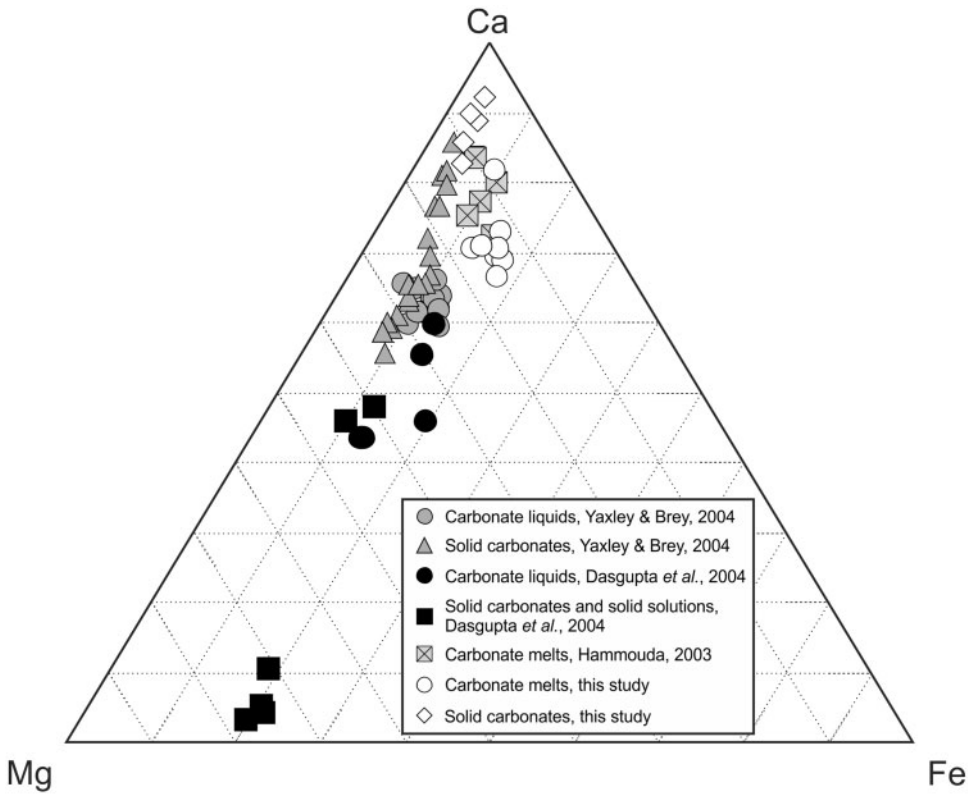

Fig. 6. Comparison of the solid carbonate and carbonate liquid compositions in this and previous studies.

capsule. The formation of the high-degree silicate melt is accounted for by the thermal gradient owing to the large capsule length. This gradient also allows comparison of the immiscible and high-degree silicate melts. Because of the small size of the pocket with two immiscible melts, it is not possible to obtain the precise composition for some elements (Ca, Mg for silicate immiscible melt and Si for carbonate immiscible melt). Nevertheless, these melts follow the general trend of melt evolution with temperature in the Pt–Gr experiments. It is evident that the silicate immiscible melt has a higher Si content (about 57·0 compared with 38·6 wt % SiO_2) and K content (1·64 compared with 0·75 wt % K_2O), and much lower amounts of Mg, Ca and Fe compared with the high-degree silicate melt (i.e. those elements that partition into the carbonate immiscible melt). The carbonate immiscible melt is calcio-dolomitic with 0·78 wt % P_2O_5, 0·20 wt % K_2O and 1·69 wt % TiO_2.

Phase proportions

Phase proportions (Fig. 9) were determined from mass-balance calculations based on the textural and compositional characteristics of the products of the experiments. The correlation between melt fraction and the type of the melt for the 3·5 and 5·0 GPa runs is illustrated in Fig. 10. For the Pt–Gr runs low-degree Si melts are formed below 10% melting and coexisting carbonate and silicate melts were observed within the narrow melting degree interval between 13 and 18%. Silicate–carbonate melts were detected at all pressures in the Pt–Gr runs with 18–29% melting and in one run (G1300.5Au–Pd) with 17% melting. High-degree silicate melts were observed only in the Pt–Gr runs at 3·5 GPa at degrees of melting above about 35%.

DISCUSSION

Evolution of the melts as a function of pressure and temperature

Experiments in Pt–Gr capsules

One of the main results of this study was the formation of four types of melt within the *P–T* range of the experiments in Pt–Gr capsules: low-degree silicate melts, immiscible carbonate and silicate melts, silicate–carbonate melts and high-degree silicate melts. The compositions of the GA1+10%cc melts change gradually over the range of applied *P–T* (Figs 7a–d and 10). Owing to the presence of

Table 6: Compositions of experimental melts

	GA1 + 10%cc in Pt-Gr													
T (°C):	1100	σ	1100	σ	1200	σ	1250	σ	1350	σ	1400	σ	1050	σ
P (GPa):	3·5		3·5		3·5		3·5		3·5		3·5		4·5	
Type of melt:	Im_{Carb}		Im_{Si}		Si-Carb		High-Si		High-Si		High-Si		Low-Si	
n:	4		4		8		12		10		10		7	
SiO_2	0·97	0·9	56·71	0·5	42·02	1·9	42·17	1·5	43·80	0·5	45·29	0·2	60·16	2·6
TiO_2	2·12	0·7	1·77	0·1	3·43	0·1	2·89	0·1	1·71	0·0	1·68	0·1	0·96	0·1
Al_2O_3	0·48	0·1	14·00	0·2	12·89	0·5	13·02	0·4	14·82	0·1	14·64	0·2	12·14	0·7
FeO	8·21	1·1	2·14	0·2	3·05	0·2	9·81	0·3	9·76	0·2	9·20	0·3	1·34	0·7
MnO	0·19	0·2	b.d.l.	–	b.d.l.	–	0·10	0·1	0·14	0·0	0·16	0·1	b.d.l.	–
MgO	4·28	0·4	0·53	0·0	2·55	0·2	3·40	0·2	5·77	0·1	6·15	0·1	0·44	0·3
CaO	28·40	1·4	2·49	0·1	9·38	0·6	11·29	0·3	11·87	0·2	13·01	0·2	1·72	1·3
Na_2O	1·32	0·6	1·98	0·3	2·89	0·0	3·58	0·4	3·81	0·1	3·49	0·1	1·31	0·2
K_2O	3·00	1·2	7·74	0·3	1·89	0·2	1·30	0·1	0·61	0·0	0·47	0·0	9·13	1·1
P_2O_5	2·91	0·7	0·37	0·0	0·75	0·1	0·46	0·1	0·35	0·1	0·24	0·1	0·75	0·6
CO_2*	48·12	0·0†	12·27	0·3	21·14	3·5	11·99	2·6	7·37	0·8	5·68	0·8	12·00	0·0
Total	100·00		100·00		100·00		100·00		100·00		100·00		100·00	
Element ratios														
Ca-no.	69·68		50·83		61·26		47·68		43·13		45·26		50·96	
Mg-no.	48·15		30·65		59·82		38·14		51·33		54·37		37·02	
CaO/SiO_2	29·32		0·04		0·22		0·27		0·27		0·29		0·03	
K_2O/Na_2O	2·27		3·92		0·65		0·36		0·16		0·13		6·95	

	GA1 + 10%cc in Pt-Gr													
T (°C):	1150	σ	1150	σ	1050	σ	1100	σ	1100	σ	1150	σ	1150	σ
P (GPa):	4·5		4·5		5		5		5		5		5	
Type of melt:	Im_{Carb}		Im_{Si}		Low-Si		Im_{Carb}		Im_{Si}		Im_{Carb}		Im_{Si}	
n:	4		3		4		12		2		4		4	
SiO_2	0·59	0·3	61·80	1·1	57·72	1·3	2·57	2·6	56·84	0·6	3·81	2·0	51·82	0·7
TiO_2	2·07	0·5	1·77	0·1	1·27	0·1	0·31	0·6	1·26	0·2	3·40	1·6	3·01	0·2
Al_2O_3	0·37	0·1	12·96	0·1	11·73	0·2	0·39	0·4	12·30	0·1	0·98	0·4	10·43	0·2
FeO	9·72	0·7	2·01	0·1	1·09	0·2	5·83	1·3	1·35	0·3	8·00	0·4	3·36	0·4
MnO	0·20	0·0	b.d.l.	–	b.d.l.	–	b.d.l.	–	b.d.l.	–	b.d.l.	–	b.d.l.	–
MgO	4·56	0·1	0·55	0·0	0·31	0·0	3·02	2·6	0·35	0·1	3·76	0·5	0·87	0·1
CaO	31·48	1·1	1·89	0·3	0·95	0·2	40·45	5·6	1·48	0·3	31·67	2·2	4·51	0·1
Na_2O	0·76	0·3	0·88	0·1	1·11	0·1	0·45	0·5	1·65	0·1	1·42	0·5	1·72	0·3
K_2O	2·77	0·7	7·62	0·1	10·50	1·1	0·54	0·9	10·20	0·1	2·61	0·9	7·94	1·1
P_2O_5	3·30	0·5	0·22	0·0	0·32	0·2	1·36	2·4	0·57	0·0	2·27	0·5	0·31	0·1
CO_2	44·21	0·4	10·24	0·8	15·00	0·00	45·08	0·00	14·00	0·00	42·09	2·60	16·02	0·60
Total	100·00		100·00		100·00		100·00		100·00		100·00		100·00	
Element ratios														
Ca-no.	69·32		44·86		42·50		82·20		49·09		73·41		54·02	
Mg-no.	45·54		32·68		33·55		48·03		31·38		45·58		31·68	
CaO/SiO_2	53·35		0·03		0·02		15·72		0·03		8·31		0·09	
K_2O/Na_2O	3·64		8·66		9·48		1·20		6·17		1·83		4·61	

(*continued*)

Table 6: Continued

	GA1 + 10%cc in Pt-Gr													
T (°C):	1200	σ	1200	σ	1250	σ	1250	σ	1300	σ	1250	σ	1250	σ
P (GPa):	5		5		5		5		5		5·5		5·5	
Type of melt:	Im_{Carb}		Im_{Si}		Im_{Carb}		Im_{Si}		Si-Carb		Im_{Carb}		Im_{Si}	
n:	4		5		6		5		9		7		2	
SiO_2	14·75	1·2	42·65	5·1	17·45	3·2	37·48	2·8	37·09	0·6	11·92	2·8	28·21	0·4
TiO_2	3·27	1·9	2·49	1·1	2·66	1·4	3·10	1·6	4·48	0·1	3·98	0·9	4·32	0·5
Al_2O_3	2·06	0·3	5·99	1·9	2·73	0·4	7·36	1·6	9·02	0·2	2·45	0·4	6·34	0·2
FeO	6·01	0·7	5·07	1·2	7·07	0·8	6·05	1·4	10·03	0·3	9·08	1·4	8·24	0·6
MnO	0·12	0·1	0·10	0·1	0·12	0·1	b.d.l.	–	0·12	0·1	0·19	0·1	b.d.l.	–
MgO	4·58	0·3	2·42	0·6	3·57	0·9	3·43	1·5	3·66	0·2	4·73	1·0	3·71	0·0
CaO	26·82	1·7	16·24	5·0	25·44	1·8	15·36	2·1	15·87	0·5	27·45	2·2	17·72	1·0
Na_2O	0·49	0·1	1·55	0·9	0·53	0·2	2·07	1·2	3·01	0·3	1·46	0·3	1·80	0·1
K_2O	1·29	0·2	2·78	0·2	1·54	0·3	2·67	1·4	1·52	0·6	2·00	0·5	3·47	0·1
P_2O_5	0·60	0·2	0·70	0·2	0·81	0·2	0·47	0·3	0·94	0·2	1·74	0·4	1·14	0·1
CO_2	40·00	0·00	20·00	0·00	38·09	2·0	22·02	0·00	14·26	0·7	35·00	0·0	25·05	0·0
Total	100·00		100·00		100·00		100·00		100·00		100·00		100·00	
Element ratios														
Ca-no.	70·79		68·92		70·83		61·81		55·12		66·77		60·45	
Mg-no.	57·60		45·95		47·37		50·24		39·38		48·12		44·53	
CaO/SiO_2	1·82		0·38		1·46		0·41		0·43		2·30		0·63	
K_2O/Na_2O	2·64		1·80		2·92		1·29		0·51		1·36		1·92	

	GA1 + 10%cc in Au-Pd				GA1 + 10%cc in Au-Pd + H_2O					
T (°C):	1225	σ	1300	σ	1250	σ	1250	σ	1250	σ
P (GPa):	5		5		5		5		5	
Type of melt:	Low-Carb		Si-Carb		Im_{Carb}		Im_{Si}		High-Si	
n:	6		6		5		4		5	
SiO_2	1·25	0·0	35·72	4·8	3·38	1·8	56·96	5·8	38·55	0·2
TiO_2	0·38	0·3	3·17	0·6	1·69	0·3	1·36	0·4	2·28	0·1
Al_2O_3	0·58	0·1	8·27	1·5	1·33	0·5	8·57	0·8	10·85	0·0
FeO	7·59	0·2	5·62	1·0	6·22	0·4	1·74	0·2	6·76	0·2
MnO	0·30	0·2	b.d.l.	–	b.d.l.	–	b.d.l.	–	0·10	0·0
MgO	5·02	0·4	2·37	0·6	4·65	0·9	0·86	0·5	3·94	0·0
CaO	32·02	2·2	14·25	3·0	33·17	1·0	4·05	2·6	13·88	0·3
Na_2O	0·41	0·1	1·26	0·8	1·49	0·6	1·87	0·5	2·88	0·1
K_2O	1·18	0·2	3·60	1·1	0·20	0·1	1·64	0·4	0·75	0·0
P_2O_5	2·40	0·0	0·33	0·2	0·78	0·1	b.d.l.	–	0·26	0·0
CO_2	48·91	2·6	25·43	3·8	47·10	3·7	22·95	5·3	19·77	0·2
Total	100·00		100·00		100·00		100·00		100·00	
Element ratios										
Ca-no.	71·28		64·97		74·55		61·32		56·34	
Mg-no.	54·07		42·93		57·10		46·94		50·94	
CaO/SiO_2	25·61		0·40		9·82		0·07		0·36	
K_2O/Na_2O	2·91		2·85		0·13		0·88		0·26	

Low-Si, low-degree silicate melt; Low-Carb, low-degree carbonate melt; Im_{Carb}, immiscible carbonate melt; Im_{Si}, immiscible silicate melt; Si-Carb, silicate–carbonate melt; High-Si, high-degree silicate melt.
*CO_2 content was calculated from the mass-balance calculations and EDS totals.
†The normalized values of melts totals have 0·0 standard deviation for CO_2, compared with those that have not been normalized.

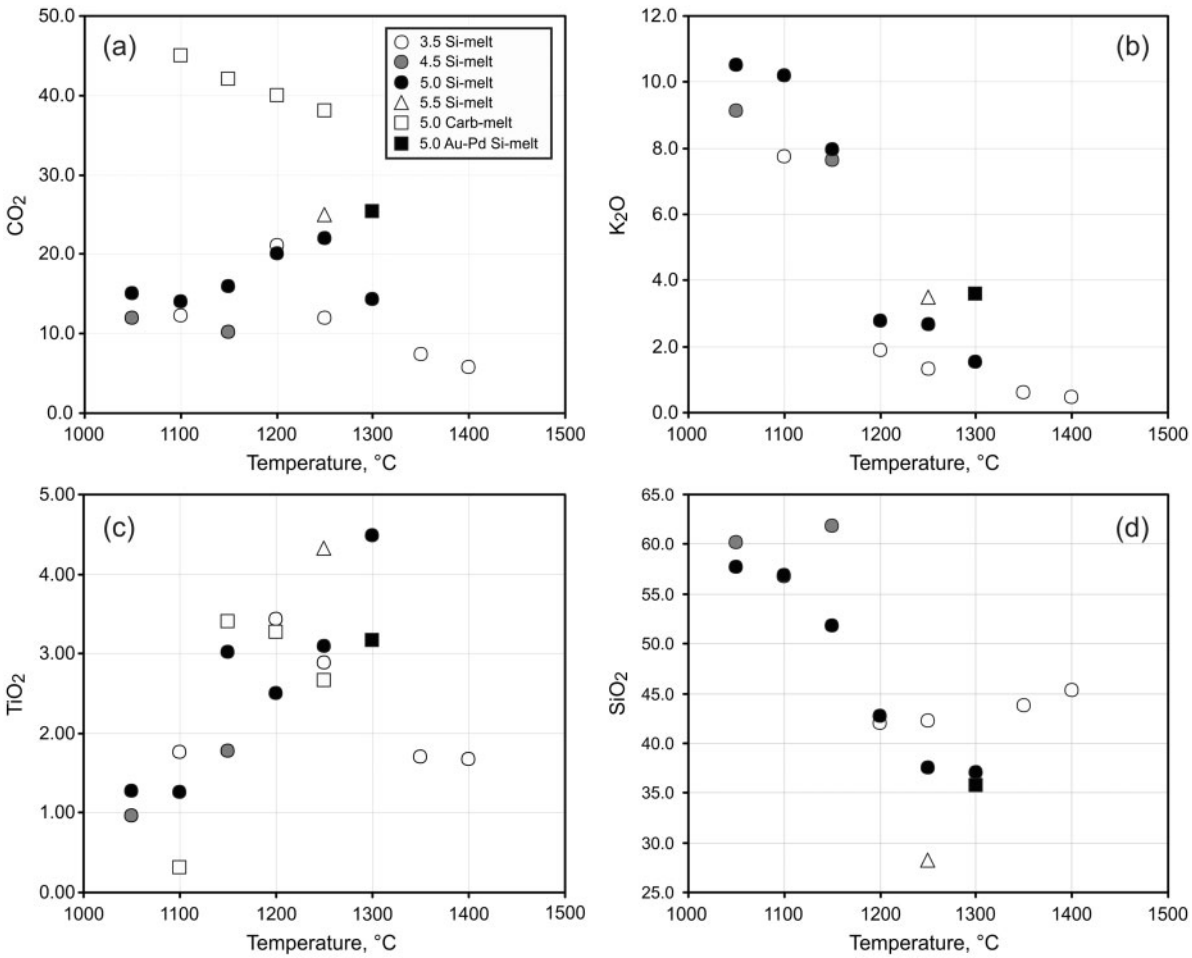

Fig. 7. Experimental melt compositions (wt %) as a function of temperature and pressure: (a) CO_2; (b) K_2O; (c) TiO_2; (d) SiO_2. The number in the legend indicates the experimental pressure in GPa. All the data correspond to GA1 +10%cc runs in Pt–Gr capsules except '5.0 Au–Pd Si-melt', which corresponds to values for silicate melt in Au–Pd capsule runs.

Na, K, CO_2, P and Ti in the starting material, the low-degree melts are strongly influenced by the melting of the accessory phases, such as K-feldspar, apatite, carbonate and rutile. K-feldspar is inferred to be the major contributing phase to the initial melts, consistent with K_2O abundances of between 9 and 11 wt %. Contributions to the low-degree Si-rich melt from rutile and apatite result in significant Ti and P abundances (around 1 wt % TiO_2 and up to 0·75 wt % P_2O_5). In addition, the melts contain up to 15% volatiles (calculated by mass balance), with the CO_2 being derived from carbonate dissolution in the low-fraction siliceous melts (Fig. 7a).

With increasing temperature, more carbonate progressively dissolves in the liquid reaching the point of CO_2 saturation and resulting in the formation of silicate melt–carbonate melt immiscibility. This is a remarkable feature of the melt evolution and its textural and compositional features are in a good agreement with recent experimental studies on H_2O-undersaturated (Hammouda, 2003) and nominally anhydrous (Dasgupta *et al.*, 2006; Gerbode & Dasgupta, 2010) carbonated eclogites. Dasgupta *et al.* (2006) observed a large field of two immiscible liquids between 1225°C and 1375°C at 3·0 GPa, which corresponds to 15–66% melting. Similar results were reported by Gerbode & Dasgupta (2010), with carbonate and silicate melts coexisting at 2·9 GPa from 1245–1275°C to 1345–1375°C, which corresponds to 34–44% melting. However, in contrast to these two studies, where silicate and carbonate melts were completely physically separated from each other in the experimental capsules with silicate melt in the top of the capsule and carbonate melt forming interstitial melt pools distributed throughout the mineral assemblage, in the current study the melts usually occur together in the same area (Fig. 3a–f), except for the G1250.5Au–PdH_2O experiment where the textures are almost identical with those presented by Gerbode &

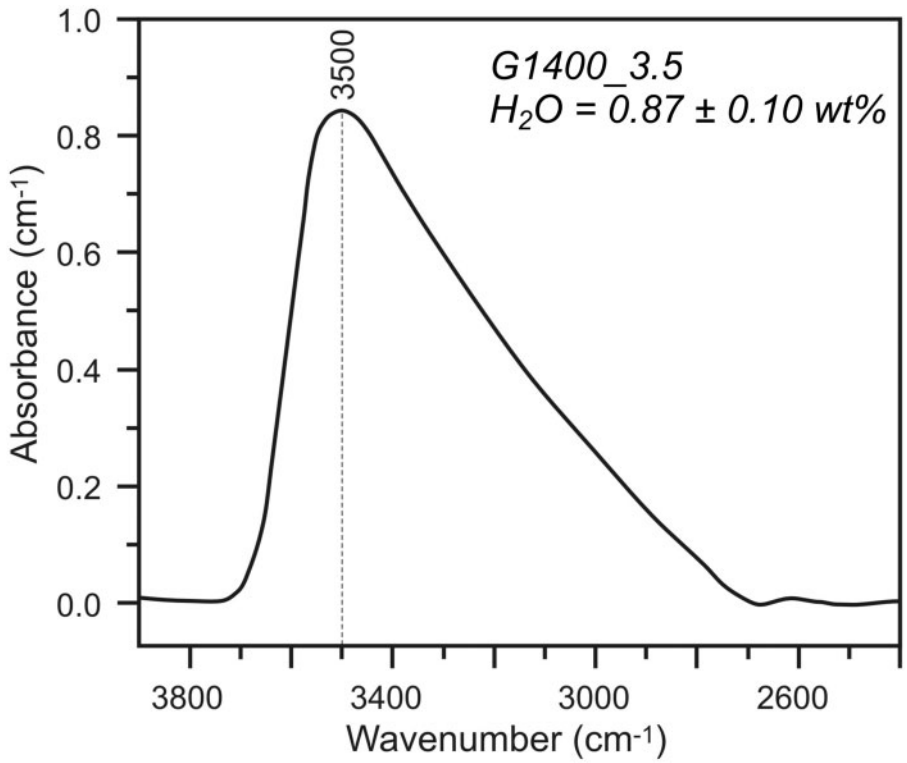

Fig. 8. Background subtracted infrared spectrum of H_2O-bearing glass. Spectrum has been scaled to a constant sample thickness of 100 μm. Glass sample shown is G1400.3.5 (estimated density is $2{\cdot}7 \pm 0{\cdot}1$ g cm^{-3}, integrated absorbance is 418 ± 9 cm^{-2}, $C_{H2O} = 0{\cdot}87 \pm 0{\cdot}10$ wt %).

Dasgupta (2010). In addition, Thomsen & Schmidt (2008) reported liquid immiscibility in an experimental study of H_2O-bearing, K-rich, carbonated pelites. They observed the coexistence of both carbonate and silicate melts at 3·7 and 5·0 GPa and 1100°C. Immiscible liquids in our experiments show regular compositional trends with increasing temperature (Fig. 11). Our data are in very good agreement with all the other data on alkali-poor carbonated eclogites, although compared with the other studies, the silicate and carbonate immiscible melts at lower temperatures in GA1+10%cc are very strongly shifted toward the Si + Al and Ca + Mg + Fe apices in Fig. 11.

The early immiscible silicate melt at 1100°C and 5·0 GPa has a similar K-rich composition to the single silicate melt at 1050°C and 5·0 GPa, which can be well explained by the presence of solid calcitic carbonate at 1050°C in equilibrium with highly siliceous K-rich melt. By melting, carbonate does not contribute to the silicate melt and its composition changes very little. We observe a gradual change in the compositions of the immiscible melts with increasing temperature (Fig. 11), whereas in the other studies the immiscible melts do not seem to have strong compositional variations.

With increasing temperature, at higher degrees of melting (around 15–20%), the immiscibility gap closes over a solvus and a single silicate–carbonate melt is formed. Owing to the presence of a substantial amount of CO_2 (14–21 wt %), this melt is depleted in SiO_2 (37–42 wt %) compared with low-degree Si melts (58–60 wt % SiO_2). Thus, in contrast to the common statement that the amount of SiO_2 in melts always increases with temperature at a given pressure (Yaxley & Brey, 2004; Litasov & Ohtani, 2010), the melting behaviour of GA1+10%cc in Pt–Gr capsule exhibits different trends. The amount of SiO_2 in the silicate melt constantly decreases from low degrees of melting to the closure of the immiscibility gap (18% of melting) and thereafter increases with increasing degrees of melting.

High-degree melts are dominated by cotectic melting of only garnet and clinopyroxene. This is in a good agreement with the CO_2 trend of the melts (Fig. 7a). The amount of CO_2 in the melt gradually increases until major silicate phases start melting, contributing silicate components and dissolving carbonate. Therefore the melt compositions do not vary significantly and the concentration of incompatible elements in the melt decreases as they become more diluted by components from the major phases. Because of the substantial amount of volatiles in the high-degree melts (6–12% CO_2 and inferred 0·8–1·0% H_2O), they are relatively low in SiO_2

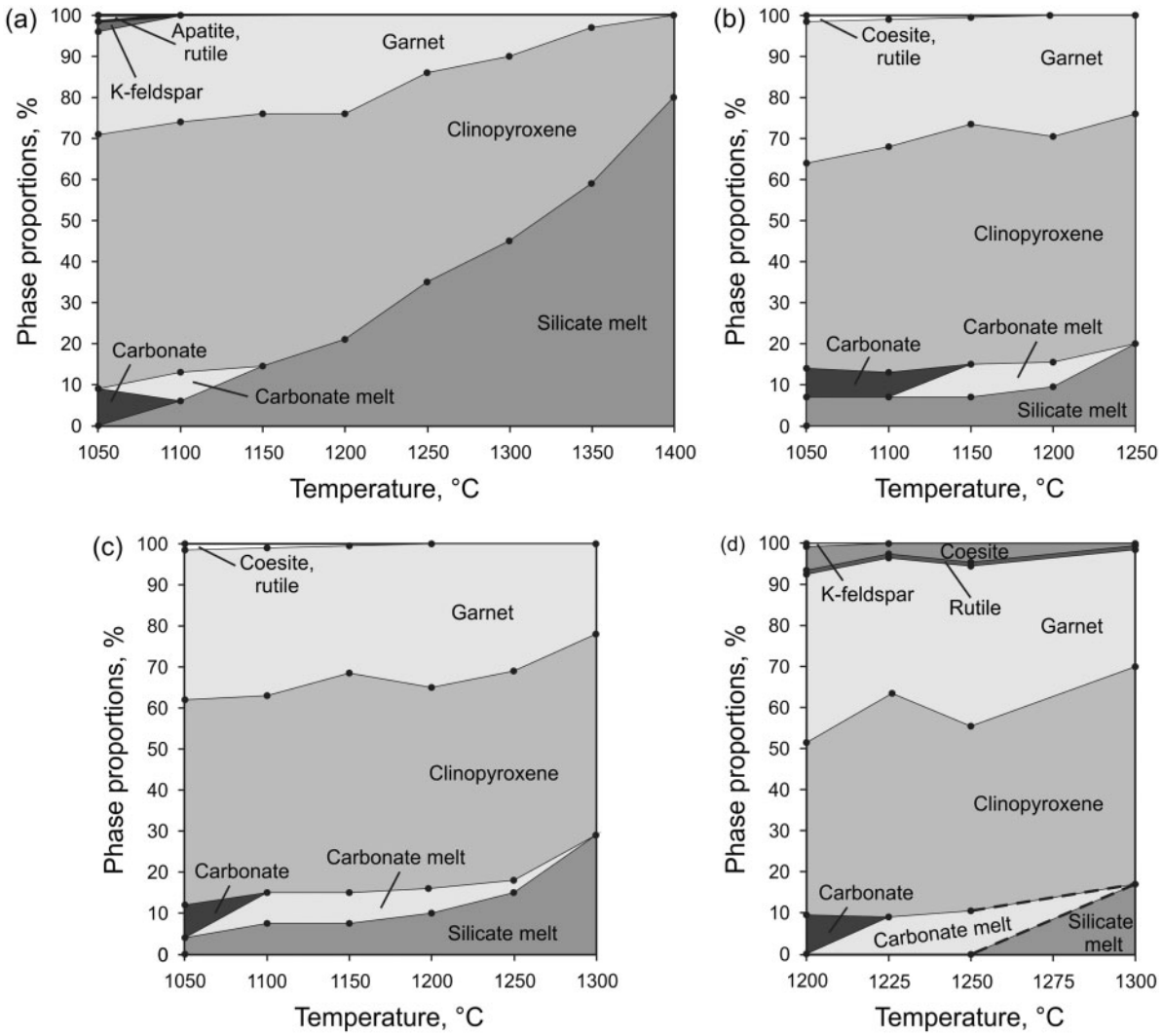

Fig. 9. Phase proportions in weight per cent of the observed phases at all the investigated pressures (GPa): (a) 3·5 GPa, (b) 4·5 GPa and (c) 5·0 GPa in Pt–Gr; (d) 5·0 GPa in Au–Pd capsules. Dashed lines in (d) show inferred values.

(42–45 wt %), corresponding to basaltic or even tephritic compositions, and are similar to the high-degree silicate melt composition reported by Dasgupta *et al.* (2006).

Experiments in Au–Pd capsules

Melt evolution in the experiments in Au–Pd capsules follows similar patterns to those previously reported for anhydrous carbonated eclogites (Yaxley & Brey, 2004), evolving from carbonatitic to siliceous with an increase of SiO_2 content over the whole interval of melting. We infer that in the Au–Pd experiments the major phases that contribute to the lowest degree melts are K-feldspar and carbonate. Melting temperatures of K-feldspar and carbonate are similar; therefore it is difficult to suggest which of these phases was the first to contribute to the melt. As the amount of carbonate in the system is much higher than the amount of K-feldspar, early melts are carbonatitic. Their SiO_2 content progressively increases with increasing degree of melting, as garnet and clinopyroxene contribute increasingly to the melt. The amount of TiO_2 in the silicate–carbonate melts is higher than in the low-degree carbonate melt (3·17 vs 0·38 wt % TiO_2), which suggests that rutile melts mainly at intermediate degrees of melting.

The effect of the capsule material on solidus temperatures

For this study we distinguish two solidi: silicate and carbonate. In the experiments in Pt–Gr capsules the silicate solidus is below the carbonate solidus at 4·5 and 5·0 GPa and not resolvable from the carbonate solidus at

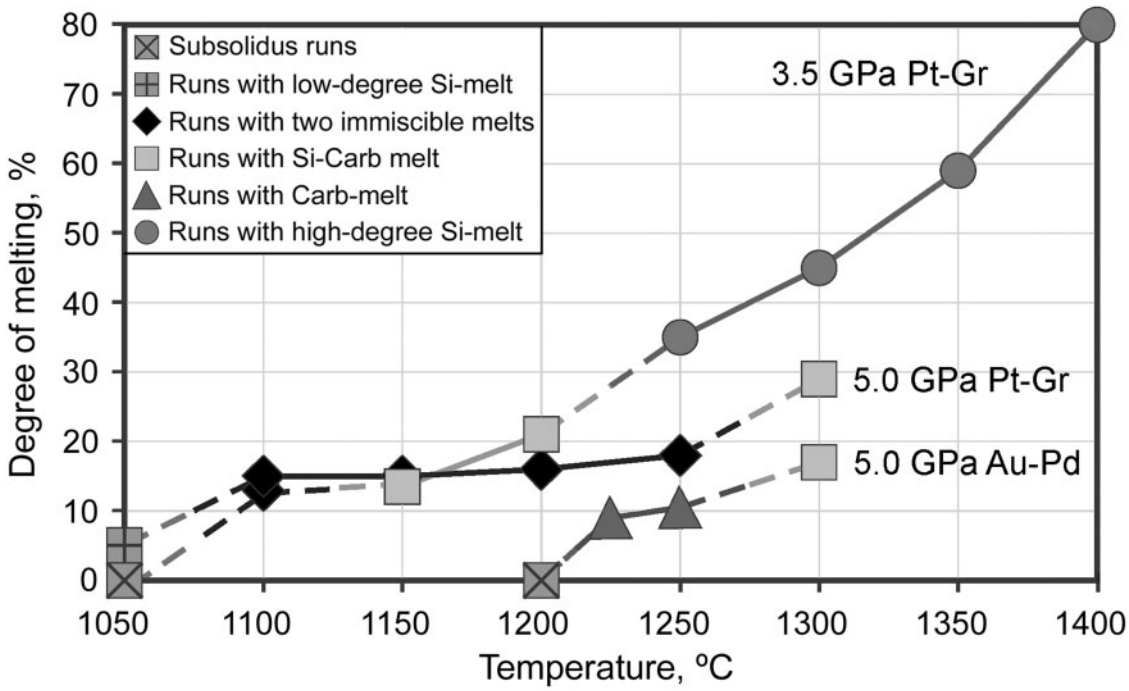

Fig. 10. The evolution of melt composition with temperature at pressures of 3·5 and 5·0 GPa in Pt–Gr capsules and 5·0 GPa in Au–Pd capsules.

3·5 GPa and 1075°C. It is likely that a difference in silicate and carbonate solidus temperatures at 3·5 GPa exists; however, it must be less than 50°C. The temperatures of the carbonate solidus lie between 1050 and 1100°C at 3·5 and 5·0 GPa and between 1100 and 1150°C at 4·5 GPa. The carbonate solidus in Au–Pd capsules lies between 1200 and 1225°C at 5 GPa.

The most striking results from our study are (1) the differences in near-solidus melts between the experiments conducted using the different capsule materials (potassic siliceous melt in Pt–Gr vs carbonatite melt in Au–Pd) and (2) the significant difference of at least 100°C between the estimated carbonate solidus temperatures at 5·0 GPa in experiments conducted using Pt–Gr capsules and those using Au–Pd capsules. We now explore possible reasons for these contrasting melting behaviours.

Although extensive efforts were made to minimize hydration of the mixes and experimental components during preparation of the assemblies, it is likely that during our relatively long-duration runs, hydrogen diffused into the Pt capsules and produced H_2O (Brooker *et al.*, 1998) by reaction with CO_2 or FeO. To test this hypothesis we used FTIR spectrometry and measured 0·87 wt % H_2O in the quenched glass from run G1400.3.5, which suggests the presence of about 0·5 wt % H_2O in our experiments. The presence of H_2O can significantly affect melting and phase relationships and decrease the solidus temperature even in these relatively low amounts (Green *et al.* 2010).

To minimize the effect of hydrogen penetration into the capsule and hydration of the sample, experiments were made in Au–Pd capsules. Au–Pd capsules permit less H diffusion than Pt under experimental conditions (Hall *et al.*, 2004; Nishihara *et al.*, 2006). Elevated permeability of Pt capsules has also been observed by Laporte *et al.* (2004). Chou (1986) showed that the addition of Au to platinum group elements (Pt or Pd) will decrease its permeability to hydrogen, although he concluded that at temperatures above 600–700°C at 0·2 GPa all of the metallic capsules are still permeable to H. The dramatic difference between the results in two different capsules with GA1+10%cc apparently indicates either different permeability of Pt and Au–Pd for H or possible redox reactions caused by the presence of graphite in the Pt capsules.

An estimation of the effect of the inferred amount of H_2O on the solidus temperatures by comparison with previous studies of the GA1 composition is described below (Fig. 12). The silicate solidus temperature that we detect at any investigated pressure for the Pt–Gr capsule experiments is one of an infinite array of H_2O-undersaturated solidi, which decrease in temperature with increasing H_2O content from the inferred anhydrous GA1+10%cc carbonate solidus (the Au–Pd experiments) towards the H_2O-saturated solidus of GA1+10%cc as determined by Yaxley & Green (1994). This assumption has been proved by the experiment in a Au–Pd capsule with deliberately added H_2O, in which immiscible

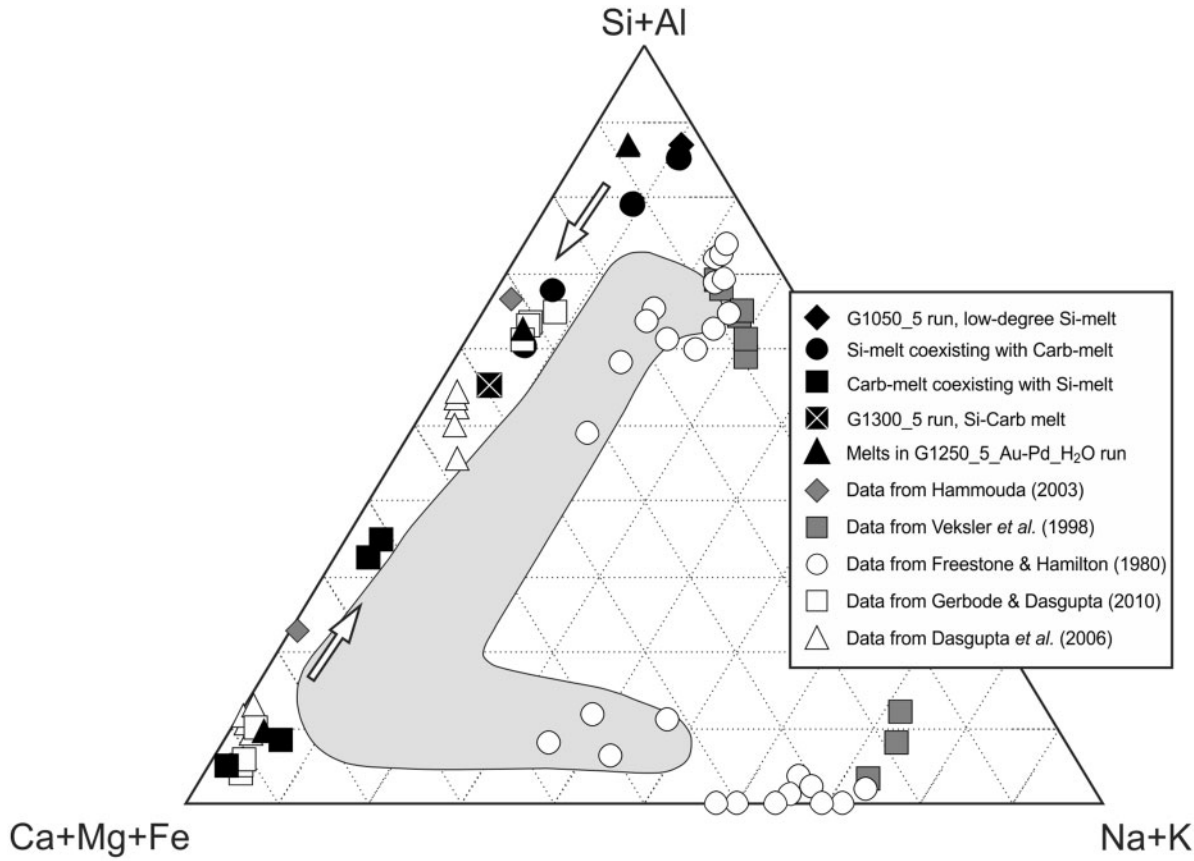

Fig. 11. Immiscible melt compositions in this and literature studies. Black symbols indicate compositions obtained in this study for the experimental runs in Pt–Gr capsules at 5 GPa. Grey and open symbols represent the compositions of immiscible melts obtained in other studies. Grey field represents the compositions of Cl-poor fluid and melt inclusions from Siberian kimberlite pipes after Zedgenizov *et al.* (2011). Arrows show the change in melt compositions in this study with increasing temperature. All the data are in moles: molar ($SiO_2 + Al_2O_3$), molar ($CaO + MgO + FeO$), molar ($Na_2O + K_2O$). Additional data are taken from Freestone & Hamilton (1980), Veksler *et al.* (1998), Hammouda (2003), Dasgupta *et al.* (2006) and Gerbode & Dasgupta (2010).

carbonate and silicate melts were formed at 5 GPa and 1250°C and the degree of melting was near 50%. This demonstrates that liquid immiscibility for the GA1+10%cc composition at 3·5–5·0 GPa is valid only for the high H_2O/CO_2 ($\sim \geq 0{\cdot}1$) ratios in the system.

Although many studies have demonstrated depression of the eclogitic solidus under hydrous conditions, to our knowledge the present study is the first demonstration that the carbonate solidus under the influence of minor amounts of water in the system is also lowered in temperature. This can have a major impact on the melting relations of carbonated eclogite, inferred to be present in the upper mantle.

Comparison with previous studies

Eclogite melting has been investigated experimentally by many researchers. Previous studies focused on the following basaltic systems: H_2O-saturated and carbonate-free, H_2O-saturated and carbonate-bearing, H_2O-free and carbonate-free, and H_2O-free and carbonate-bearing. A comparison of the solidi obtained in some of these earlier studies is made in Fig. 12.

The H_2O-saturated, CO_2-free basaltic solidus was located at 700–800°C at pressures less than 3 GPa by Lambert & Wyllie (1972). At higher pressures, the slope of the solidus in different studies varies significantly. The solidus temperature at 5 GPa was extrapolated to around 800°C by Lambert & Wyllie (1972); however, Kessel *et al.* (2005*b*) placed it at 1000–1050°C. Both studies reported silica-rich initial melts with a substantial Na_2O content. With increasing degree of melting at 4·0–6·0 GPa, Kessel *et al.* (2005*b*) observed a change in melt composition from rhyolitic at 800–1000°C to andesitic or trachytic and basaltic at 1300–1400°C.

There are only three reported studies on H_2O-saturated, CO_2-bearing basaltic compositions (Yaxley & Green, 1994; Molina & Poli, 2000; Poli *et al.*, 2009); only Yaxley & Green (1994) focused on the supra-solidus mineral

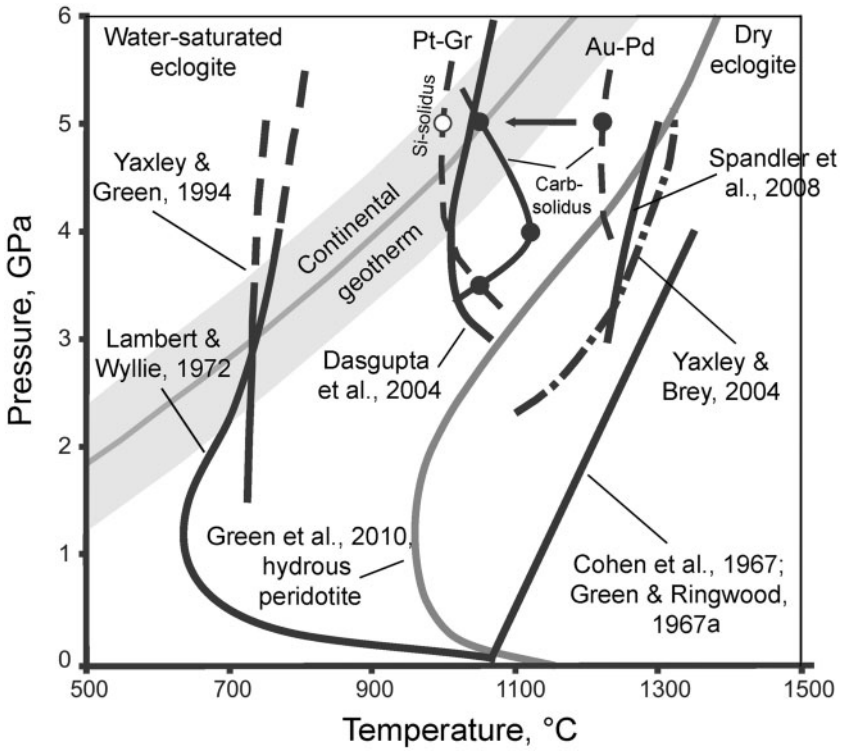

Fig. 12. The comparison of solidus temperatures for different bulk compositions. All the eclogite solidi are shown with black lines. Filled circles, estimated solidus for GA1 +10%cc; open circle, inferred solidus for GA1 +10%cc. Continuous lines and the solidus by Yaxley & Brey (2004) are reported solidi; dashed lines are inferred (speculated) solidi. Data from Cohen *et al.* (1967), Green & Ringwood (1967*a*), Lambert & Wyllie (1972), Yaxley & Green (1994), Dasgupta *et al.* (2004) and Spandler *et al.* (2008). Grey line is the conductive geotherm for a 40 mW m^{-2} heat flow from Chapman & Pollack (1977). Grey area indicates estimated geotherm values for 35–45 mW m^{-2} heat flow. Dark grey line is wet peridotite solidus from Green *et al.* (2010). Data from this study define two carbonate solidi in the runs in Pt–Gr and Au–Pd capsules, and one silicate solidus in the runs in Pt–Gr capsules.

assemblages at 1·5–3·5 GPa. That study reported the solidus to be at similar temperatures to the H_2O-saturated, CO_2-free basaltic solidus of Lambert & Wyllie (1972). The melts were broadly dacitic at low degrees of melting <850°C, and changed to andesitic melts at higher degrees of melting at >900°C at all pressures. Carbonate behaved as a refractory phase.

The solidus of H_2O- and carbonate-free basaltic assemblages has been described in many studies (Cohen *et al.*, 1967; Green & Ringwood, 1967*b*; Yasuda *et al.*, 1994; Pertermann & Hirschmann, 2003; Spandler *et al.*, 2008, and references therein). The most relevant results with regard to the present study were reported by Spandler *et al.* (2008), who used a carbonate- and H_2O-free composition almost identical to GA1. Those workers observed a solidus at much higher temperatures (1230–1300°C) than for any of the H_2O-bearing compositions and around 100°C higher than the GA1+10%cc solidus in Au–Pd capsule at 5 GPa. The low-degree melt compositions varied from high-K dacitic to basaltic andesite. High-degrees melts at >1350–1400°C at 3·0–5·0 GPa are broadly basaltic.

The solidus of nominally H_2O-free, carbonated eclogite has also been reported in several studies (Dasgupta *et al.*, 2004; Yaxley & Brey, 2004; Gerbode & Dasgupta, 2010). Two of the solidi are at ~1025°C and ~1060°C at 2·9 and 3·0 GPa respectively (Dasgupta *et al.*, 2004; Gerbode & Dasgupta, 2010), matching our inferred H_2O-present GA1+10%cc solidus in Pt–Gr capsules. The solidus determined by Yaxley & Brey (2004) is at higher temperatures, around 1150°C at 2·7 GPa. The solidus shapes also contrast (Hammouda, 2003; Dasgupta *et al.*, 2004; Yaxley & Brey, 2004). Thus, in contrast to the H_2O-saturated systems, with relatively similar reported results, little agreement is apparent on the shapes of the solidi and temperatures for nominally anhydrous carbonate-bearing basaltic compositions. There are several possible reasons for this controversy. First, it is particularly difficult to perform fully anhydrous experiments, and even small amounts of H_2O would significantly influence the solidus (Rosenthal, 2010), although the possible presence of water was not investigated or reported in those studies. Second, and more likely, in addition to a possible influence of H_2O, the

nature of the carbonated eclogite solidus also depends on bulk composition, particularly the following parameters: SiO_2 content, CaO/MgO and alkali oxides/CO_2 ratios, and total alkali abundances (especially K_2O). The effect of the starting composition on the carbonated eclogite solidus has been summarized by Dasgupta *et al.* (2005), who suggested that the Ca/Mg ratio of the carbonated portion of the whole-rock, the bulk Na_2O/CO_2 ratio, and the presence of H_2O are of principal importance. Apart from these parameters, the importance of K_2O should also be emphasized. Our observation is that K_2O can play as important a role as an alkali component at these pressures as Na_2O does. In the highest-pressure runs (>3·0–3·5 GPa), especially at lower degrees of melting, Na behaves as a relatively compatible element and partitions into clinopyroxene because of the increased stabilization of jadeite at high pressures. On the other hand, no studies on the effect of the incompatibility of K in the carbonated eclogite system have been conducted and it is not entirely clear which phase will host potassium at around 5·0 GPa. In the simplified $KAlSi_3O_8$ or $(K,Na)AlSi_3O_8$ systems, K-feldspar was noted to be stable at least up to 6·0 GPa (Urakawa *et al.*, 1994; Yagi *et al.*, 1994), transforming at higher pressures to wadeite + kyanite + coesite. However, no experimental studies have been performed on more natural compositions and K-feldspar is destabilized in CO_2- and H_2O-free eclogitic systems at pressures of 4–5 GPa (Spandler *et al.*, 2008). Therefore we consider that in a similar fashion to H_2O, K has a significant impact on the melting temperatures and the character of the melt.

The first melts produced in CO_2-bearing and H_2O-free systems were always Na-rich calcio-dolomitic carbonatite melts with variable Ca–Mg–Fe proportions. With increasing degree of melting, either two immiscible melts were generated (Dasgupta & Hirschmann, 2006; Gerbode & Dasgupta, 2010), or the silicate component of the melt increased, gradually diluting the carbonate component (Yaxley & Brey, 2004).

The remarkable difference of our study is that GA1+10%cc in the Pt–Gr capsules yields K-rich highly siliceous liquids (broadly trachyandesitic–phonolitic compositions) at the lowest degrees of melting, which have never been reported in any previous studies of carbonated eclogites. The only other K-rich siliceous melts were observed by Spandler *et al.* (2008) in volatile-free eclogite, but their SiO_2 contents were higher (>60 wt % compared with 58–60 wt % SiO_2 for GA1+10%cc).

Depression of the silicate solidus below that of carbonate is most probably due to: (1) a relatively high H_2O/CO_2 ratio (≥0·1) of the mix in the experimental capsules, caused by contamination of the capsules by H_2O; (2) the presence of K_2O in the system. In the case of Au–Pd experiments, we infer that the amount of H_2O in the system was negligible and the character of melting is similar to that of the previously reported H_2O-free CO_2-bearing eclogites.

Implications for metasomatism in the mantle

The possibility of the subduction of carbonate into the deeper mantle has been addressed by many workers (Kerrick & Connolly, 2001; Dasgupta & Hirschmann, 2010). Based on an average subduction geotherm (Peacock, 2003) and experimental determinations of carbonated eclogite phase relations (Yaxley *et al.*, 1994; Hammouda, 2003; Dasgupta *et al.*, 2004; Yaxley & Brey, 2004), there is general agreement that at least some carbonate in altered oceanic crust can survive subduction and be carried deeper into the mantle. If this happens after dehydration or partial melting and hence removal from the system of some of the incompatible elements and some of the CO_2 dissolved in a hydrous melt or fluid, then almost anhydrous and relatively refractory carbonate-bearing eclogite will continue being subducted. The fate of such a subducted eclogite has been discussed in previous experimental studies of H_2O-free, carbonate-bearing eclogite compositions (Dasgupta *et al.*, 2004, 2005; Yaxley & Brey, 2004). The most likely scenario for most subduction geotherms will be subduction of H_2O-undersaturated carbonated eclogite without melting during the prograde path; thus, carbonated eclogite will survive subduction zone processes and will be subducted into the deeper upper mantle or beyond with some amount of H_2O stored in nominally anhydrous minerals (NAMs).

The accretion of subducted oceanic lithospheric slabs has been suggested as one possible mechanism for the formation of cratonic lithosphere (Canil, 2004; Helmstaedt, 2009). Cratons are relatively cold, thick, and chemically depleted. They are often considered to have been tectonically inactive for billions of years, but in fact there are abundant signs of continuing activity (Foley, 2008). The genesis of kimberlites, which are strongly associated with cratonic environments, is one manifestation of this. Kimberlite-hosted mantle xenoliths and inclusions in diamond, which are fragments of the cratonic lithosphere, often exhibit features of relatively recent metasomatism (Pyle & Haggerty, 1998; Jacob *et al.*, 2000). Detailed study of mantle xenoliths from the Slave Craton and Greenland (Canil, 2004, and references therein; Gaffney *et al.*, 2007) coupled with geophysical evidence that reveals the stacking of subducted slabs (Bostock, 1998) suggests that subducted slabs, presumably containing carbonate-bearing eclogite (former altered oceanic crust), can be eventually incorporated into stabilized, peridotite-dominated cratonic lithosphere. If we accept this hypothesis, then the melting relations described here may be extremely relevant to metasomatism and melt generation in the cratonic lithosphere.

Conductive mantle geotherm temperatures may vary significantly at a given pressure, depending mainly on the tectonic setting. Cratonic lithosphere typically has geotherms defined by a range of heat flows of 35–45 mW m^{-2}. Both the silicate and carbonate solidi of our H_2O-undersaturated carbonated eclogite at ≥5·0 GPa are at temperatures below or near the average cratonic geotherm for a heat flow of 40 mW m^{-2} proposed by Chapman & Pollack (1977). Thus, a body of H_2O-undersaturated carbonated eclogite may not survive thermal equilibration to cratonic mantle temperatures in the lower part of the cratonic lithosphere (~150 km) without partial melting. It is important to note that its solidus is at lower temperatures at the studied pressures (3·5–5 GPa) than the silicate solidus of a wet peridotite (Fig. 12). Therefore melt originating from the partial melting of water-undersaturated carbonated eclogite may metasomatize the surrounding peridotite. Melting of carbonated eclogite of similar composition to GAl under water-undersaturated conditions will produce K-rich and highly siliceous partial melts at low degrees of melting, and may also produce immiscible silicate–carbonate melts at higher degrees of melting. Alkali- and Si-rich melt is not expected to migrate far into the surrounding refractory peridotite, but would react with the wall-rock, causing Si enrichment with the formation of orthopyroxene, phlogopite, and pyrope-rich garnet, and consuming olivine (Sekine & Wyllie, 1982; Rapp *et al.*, 1999). However, the degree of metasomatism and the crystallization of additional phases, such as phlogopite, will be strongly affected by the melt–rock ratio and by the amount of K and H_2O in the initial eclogite. Low-viscosity carbonate immiscible melts may penetrate further into surrounding peridotite bodies (e.g. Hammouda & Laporte, 2000), causing carbonate metasomatism (described below). The solidus of anhydrous carbonate eclogite is at higher temperatures than the typical cratonic mantle geotherm. Therefore it is most likely that it will be able to thermally equilibrate with the cratonic mantle without melting (Fig. 12) and could be preserved in the cratonic lithosphere for long periods of time.

A number of processes may trigger melting of carbonated eclogite bodies in the cratonic mantle. Heating may result from local magma intrusion or more regionally from rifting. As a result of rifting processes, hot and low-density asthenospheric mantle may upwell, while the continental lithosphere is thinned. This has been investigated by multiple seismic studies of the East African (Ritsema *et al.*, 1998, and references therein), Rio Grande (Wilson *et al.*, 2005, and references therein) and other rift systems. Rifting is often accompanied by substantially increased heat flow and an enhanced geotherm, which may lead to igneous activity. Carbonated eclogite bodies in rifted cratonic lithosphere may thus reach a carbonate solidus and produce alkali-bearing carbonatitic melts at low degrees of melting.

If these carbonate melts penetrate into the surrounding peridotitic wall-rock, the carbonate melt may freeze in the wall-rock, crystallizing magnesite (or dolomite), clinopyroxene and apatite and forming metasomatized carbonated peridotite (Dasgupta *et al.*, 2004; Yaxley & Brey, 2004). A number of studies on mantle peridotites from various East African rift zones have reported the crystallization of clinopyroxene and accessory monazite and apatite, light rare earth element enrichment and high field strength element (particularly Ti) depletion of the bulk-rock as a result of metasomatic enrichment (Rudnick *et al.*, 1993; Bedini *et al.*, 1997). In some cases, penetration of carbonate-rich melts may locally lower the peridotite solidus and trigger peridotite + CO_2 partial melting, producing dolomitic carbonatites, which could migrate through and metasomatize the ambient peridotite at very low melt fractions. As mentioned by Dasgupta *et al.* (2006), multi-stage melting of heterogeneous metasomatized carbonate-rich mantle may be typical behaviour.

A second mechanism for melting of carbonated eclogite bodies included in the cratonic mantle involves fluxing by hydrous fluids generated by redox-related or other processes. Studies on the redox state of the cratonic mantle based on mantle xenoliths have led to the conclusion that the oxygen fugacity (fO_2) of the upper mantle is heterogeneous, both laterally and vertically, but generally decreases with depth reaching FMQ − 3 to FMQ − 5 log units (where FMQ is the fayalite–magnetite–quartz buffer) at about 6–7 GPa (Woodland & Koch, 2003; Foley, 2011, and references therein). Such low values of fO_2 influence the C–H–O fluid phase speciation such that CH_4 and H_2O are the major species at these depths (Ballhaus & Frost, 1994; Foley, 2011, and references therein). CH_4-rich fluids migrating from the deeper mantle (Taylor & Green, 1998; Foley, 2011) into the cratonic lithosphere may therefore encounter progressively more oxidizing conditions, eventually intersecting the carbon-saturation surface (Taylor & Green, 1998) and oxidizing according to the following reaction:

$$CH_4 + O_2 = 2H_2O + C.$$

Crystallization of diamond will be accompanied by a rapid increase in H_2O activity, which will lower the solidus temperature of both peridotite and eclogite and may cause the intersection of these solidi with the mantle geotherm, causing melting. This was described by Taylor & Green (1988) as 'redox melting'. Some subducted oceanic crust, which was not incorporated into cratons, may subduct to greater depths of 200–300 km or more without experiencing carbonate melting (Foley, 2011); this may be of particular importance for producing CH_4 and H_2 in the lower part of the upper mantle, which could thereafter

trigger the redox melting of shallower, more oxidized domains, containing carbonate (Foley, 2011).

An alternative means of introducing H_2O into carbonated eclogite bodies in the cratonic lithosphere relates to the presence of water in NAMs in peridotite or eclogite. Studies on mantle xenoliths suggest that the cratonic mantle contains significant amounts of water stored in NAMs (Bell & Rossman, 1992; Bonadiman *et al.*, 2009). The water content of olivine in the cratonic mantle usually varies between 0 and 80 ppm, depending on the degree of bulk-rock depletion and depth (the lower contents are observed in peridotite xenoliths from cratonic roots, equilibrated at above 5 GPa and 1100°C; Peslier *et al.*, 2010). However, the main host of H_2O within the cratonic lithosphere is clinopyroxene, which typically incorporates ~200–500 ppm H_2O (Bell & Rossman, 1992; Li *et al.*, 2008). This implies that bodies of eclogite, containing roughly 50% of omphacite, may have relatively high water concentrations in comparison with the surrounding peridotite. If additional accessory minerals (rutile, kyanite) are present in the eclogite, the amount of water in the bulk-rock may be significantly higher (Bell & Rossman, 1992). This study shows that low-degree partial melts of carbonated eclogites are usually dominated by melting of accessory phases. Therefore any low-degree partial melts of an eclogite will be water-rich. Water can also be liberated from the clinopyroxene during partial melting. Therefore if a part of the sub-cratonic mantle containing layers of carbonated altered oceanic crust undergoes decompression the water stored in the clinopyroxene could be liberated, triggering partial melting (Rosenthal, 2010).

In addition, Si enrichment of mantle peridotites marked by high modal abundances of orthopyroxene has been observed in xenoliths from both the African and Siberian cratons (Kelemen *et al.*, 1998). It has been suggested that the high Si/Mg ratio and high abundances of orthopyroxene cannot be generated solely by melt extraction and require an additional mechanism for SiO_2 introduction (Kelemen *et al.*, 1998; Walter, 1999; Simon *et al.*, 2007; Hin *et al.*, 2009). A positive correlation between Ni in olivine and the modal amount of orthopyroxene, observed by Kelemen *et al.* (1998), may suggest interaction of mantle peridotite with siliceous slab-derived melts as a plausible mechanism of Si enrichment (Kelemen *et al.*, 1998; Walter, 1999). Such Si-rich melts could be generated from melting of the refractory residues of carbonated eclogite after low-degree silicate and carbonate partial melts have separated and migrated through the overlying mantle.

Implications for fluid and melt inclusions in diamonds

The origins of melt and fluid inclusions in diamonds have been addressed by many workers (e.g. Klein-BenDavid *et al.*, 2007; Weiss *et al.*, 2009; Litasov *et al.*, 2010). The three major compositional end-members of the fluid and melt inclusions are: carbonatitic (enriched in carbonate, Ca, Mg and Fe); hydrous silicic (enriched in Si, Al, K and H_2O); hydrous saline (enriched in Cl, Na, K and H_2O). According to Weiss *et al.* (2009) silicic melts preserved in eclogitic diamonds from Guinea and Yakutia are near-solidus melts produced by low-degree melting of carbonate-bearing eclogite in the presence of an aqueous fluid. Although compositional similarities between silicic melts and fluid inclusions in diamonds and experimentally determined melts of H_2O-bearing eclogite (Hammouda, 2003; Kessel *et al.*, 2005*a*), and H_2O- and CO_2-bearing eclogite (Yaxley & Green, 1994) have been observed, the melts from these studies did not form a continuous compositional trend from silicate to carbonate end-members with varying degree of melting. Litasov *et al.* (2010) have argued that low-degree partial melts of H_2O-bearing Cl-free eclogite will never evolve from silica-rich towards carbonate-rich compositions but that this trend can be achieved during the melting of H_2O-free and Cl-bearing eclogitic compositions. Here we present a new model, in which the entire silicate–carbonate compositional trend may be generated in one process of melting of a K- and CO_2-bearing, H_2O-undersaturated MORB composition, which is applicable to Cl-free (or Cl-poor) inclusions in diamonds (Fig. 11). However, it is important to note that oxygen fugacity must be taken into an account when speculating about diamond formation at these P–T conditions.

CONCLUSIONS

(1) Based on the comparison between solidus temperatures and subduction geotherms H_2O-undersaturated, carbonated eclogites would survive along typical subduction P–T paths without melting.

(2) Both the silicate and carbonate solidi of carbonate-bearing, H_2O-undersaturated eclogite at cratonic lithosphere pressures are at lower temperatures than the wet solidus of peridotite. For an average mantle geotherm, at 5 GPa carbonate-bearing, H_2O-undersaturated eclogite will start melting.

(3) The lowest-degree melts of H_2O-undersaturated, carbonate-bearing MORB compositions at 3·5–5·0 GPa are K-rich, highly siliceous liquids (broadly trachyandesite–phonolite), which have not yet been reported in any previous experimental studies of carbonated eclogites.

(4) Liquid immiscibility is a consequence of the presence of minor H_2O in the system. It was observed at all investigated pressures in a narrow melting interval (13–18%) and over a temperature interval expanding with pressure from about 50°C at 3·5 GPa to >150°C at 5 GPa.

(5) Intermediate- to high-degree melts of both anhydrous and H_2O-saturated compositions are

Si-undersaturated, silicate–carbonate melts (36–45 wt % SiO_2) containing substantial dissolved CO_2 (up to about 21 % CO_2).

(6) In contrast to previous studies, the SiO_2 content of the melt can decrease with increasing degree of melting. This occurs in H_2O-undersaturated systems all the way to the closure of the immiscibility gap and can explain the variation of fluid and melt inclusions in Cl-free (or Cl-poor) diamonds.

(7) Small amounts of water from sources external to carbonated eclogite bodies (e.g. H_2O in NAMs, such as olivine) in the cratonic lithosphere may decrease not only the silicate but also the carbonate solidus of the carbonated eclogite and trigger melting at much lower temperatures than previously thought. This may result in abundant carbonatitic and alkali-rich silicate metasomatism.

ACKNOWLEDGEMENTS

We thank Dean Scott and David Clark for the technical support with experiments, and Frank Brink and Bob Rapp for the assistance with electron microprobes. This paper also benefited greatly from discussions with Aleksandr Stepanov, Laure Martin and Hugh O'Neill. Alexander Kanishchev is acknowledged for the help with figures. We are very grateful to Patrizia Fumagalli and Tahar Hammouda for thorough and penetrating reviews.

FUNDING

KK was supported by an Australian National University PhD stipend during completion of this project. The research was funded by a Australian Research Council Discovery Grant to GMY.

REFERENCES

Ballhaus, C. & Frost, B. R. (1994). The generation of oxidized CO_2-bearing basaltic melts from reduced CH_4-bearing upper mantle sources. *Geochimica et Cosmochimica Acta* **58**, 4931–4940.

Bedini, R. M., Bodinier, J. L., Dautria, J. M. & Morten, L. (1997). Evolution of LILE-enriched small melt fractions in the lithospheric mantle: a case study from the East African Rift. *Earth and Planetary Science Letters* **153**, 67–83.

Bell, D. R. & Rossman, G. R. (1992). Water in Earth's mantle: the role of nominally anhydrous minerals. *Science* **255**, 1391–1397.

Bonadiman, C., Hao, Y. T., Coltorti, M., Dallai, L., Faccini, B., Huang, Y. & Xia, Q. K. (2009). Water contents of pyroxenes in intraplate lithospheric mantle. *European Journal of Mineralogy* **21**, 637–647.

Bostock, M. G. (1998). Mantle stratigraphy and evolution of the Slave province. *Journal of Geophysical Research—Solid Earth* **103**, 21183–21200.

Boyd, F. R., Pokhilenko, N. P., Pearson, D. G., Mertzman, S. A., Sobolev, N. V. & Finger, L. W. (1997). Composition of the Siberian cratonic mantle: evidence from Udachnaya peridotite xenoliths. *Contributions to Mineralogy and Petrology* **128**, 228–246.

Brooker, R., Holloway, J. R. & Hervig, R. (1998). Reduction in piston-cylinder experiments: The detection of carbon infiltration into platinum capsules. *American Mineralogist* **83**, 985–994.

Canil, D. (2004). Mildly incompatible elements in peridotites and the origins of mantle lithosphere. *Lithos* **77**, 375–393.

Chapman, D. S. & Pollack, H. N. (1977). Regional geotherms and lithospheric thickness. *Geology* **5**, 265–268.

Chou, I. M. (1986). Permeability of precious metals to hydrogen at 2 kb total pressure and elevated temperatures. *American Journal of Science* **286**, 638–658.

Cohen, L. H., Ito, K. & Kennedy, G. C. (1967). Melting and phase relations in an anhydrous basalt to 40 kilobars. *American Journal of Science* **265**, 475–518.

Dasgupta, R. & Hirschmann, M. M. (2006). Melting in the Earth's deep upper mantle caused by carbon dioxide. *Nature* **440**, 659–662.

Dasgupta, R. & Hirschmann, M. M. (2010). The deep carbon cycle and melting in Earth's interior. *Earth and Planetary Science Letters* **298**, 1–13.

Dasgupta, R., Hirschmann, M. M. & Dellas, N. (2005). The effect of bulk composition on the solidus of carbonated eclogite from partial melting experiments at 3 GPa. *Contributions to Mineralogy and Petrology* **149**, 288–305.

Dasgupta, R., Hirschmann, M. M. & Stalker, K. (2006). Immiscible transition from carbonate-rich to silicate-rich melts in the 3 GPa melting interval of eclogite + CO_2 and genesis of silica-undersaturated ocean island lavas. *Journal of Petrology* **47**, 647–671.

Dasgupta, R., Hirschmann, M. M. & Withers, A. C. (2004). Deep global cycling of carbon constrained by the solidus of anhydrous, carbonated eclogite under upper mantle conditions. *Earth and Planetary Science Letters* **227**, 73–85.

Dixon, J. E., Stolper, E. M. & Holloway, J. R. (1995). An experimental study of water and carbon dioxide solubilities in mid-ocean ridge basaltic liquids. Part 1: Calibration and solubility models. *Journal of Petrology* **36**, 1607–1631.

Dobson, D. P., Jones, A. P., Rabe, R., Sekine, T., Kurita, K., Taniguchi, T., Kondo, T., Kato, T., Shimomura, O. & Urakawa, S. (1996). *In-situ* measurement of viscosity and density of carbonate melts at high pressure. *Earth and Planetary Science Letters* **143**, 207–215.

Ellis, D. J. & Green, D. H. (1979). Experimental study of the effect of Ca upon garnet–clinopyroxene Fe–Mg exchange equilibria. *Contributions to Mineralogy and Petrology* **71**, 13–22.

Foley, S. F. (2008). Rejuvenation and erosion of the cratonic lithosphere. *Nature Geoscience* **1**, 503–510.

Foley, S. (2011). A reappraisal of redox melting in the Earth's mantle as a function of tectonic setting and time. *Journal of Petrology* **52**, 1363–1391.

Freestone, I. C. & Hamilton, D. L. (1980). The role of liquid immiscibility in the genesis of carbonatites—an experimental study. *Contributions to Mineralogy and Petrology* **73**, 105–117.

Gaffney, A. M., Blichert-Toft, J., Nelson, B. K., Bizzarro, M., Rosing, M. & Albarede, F. (2007). Constraints on source-forming processes of West Greenland kimberlites inferred from Hf–Nd isotope systematics. *Geochimica et Cosmochimica Acta* **71**, 2820–2836.

Garlick, G. D., Macgregor, I. D. & Vogel, D. E. (1971). Oxygen isotope ratios in eclogites from kimberlites. *Science* **172**, 1025–1027.

Gerbode, C. & Dasgupta, R. (2010). Carbonate-fluxed melting of MORB-like pyroxenite at 2·9 GPa and genesis of HIMU ocean island basalts. *Journal of Petrology* **51**, 2067–2088.

Ghosh, S., Ohtani, E., Litasov, K., Suzuki, A. & Sakamaki, T. (2007). Stability of carbonated magmas at the base of the Earth's upper mantle. *Geophysical Research Letters* **34**, L22312, doi:10.1029/2007GL031349.

Green, D. H. & Ringwood, A. E. (1967*a*). An experimental investigation of gabbro to eclogite transformation and its petrological applications. *Geochimica et Cosmochimica Acta* **31**, 767–833.

Green, D. H. & Ringwood, A. E. (1967*b*). The genesis of basaltic magmas. *Contributions to Mineralogy and Petrology* **15**, 103–190.

Green, D. H., Hibberson, W. O., Kovacs, I. & Rosenthal, A. (2010). Water and its influence on the lithosphere–asthenosphere boundary. *Nature* **467**, 448–451.

Hall, L. J., Brodie, J., Wood, B. J. & Carroll, M. R. (2004). Iron and water losses from hydrous basalts contained in Au80Pd20 capsules at high pressure and temperature. *Mineralogical Magazine* **68**, 75–81.

Hammouda, T. (2003). High-pressure melting of carbonated eclogite and experimental constraints on carbon recycling and storage in the mantle. *Earth and Planetary Science Letters* **214**, 357–368.

Hammouda, T. & Laporte, D. (2000). Ultrafast mantle impregnation by carbonatite melts. *Geology* **28**, 283–285.

Helmstaedt, H. (2009). Crust–mantle coupling revisited: The Archean Slave craton, NWT, Canada. *Lithos* **112**, 1055–1068.

Helmstaedt, H., Anderson, O. L. & Gavasci, A. T. (1972). Petrofabric studies of eclogite, spinel-websterite, and spinel-lherzolite xenoliths from kimberlite-bearing breccia pipes in Southeastern Utah and Northeastern Arizona. *Journal of Geophysical Research* **77**, 4350–4365.

Hin, R. C., Morel, M. L. A., Nebel, O., Mason, P. R. D., van Westrenen, W. & Davies, G. R. (2009). Formation and temporal evolution of the Kalahari sub-cratonic lithospheric mantle: Constraints from Venetia xenoliths, South Africa. *Lithos* **112**, 1069–1082.

Jacob, D., Jagoutz, E., Lowry, D., Mattey, D. & Kudrjavtseva, G. (1994). Diamondiferous eclogites from Siberia: Remnants of Archean oceanic crust. *Geochimica et Cosmochimica Acta* **58**, 5191–5207.

Jacob, D. E. (2004). Nature and origin of eclogite xenoliths from kimberlites. *Lithos* **77**, 295–316.

Jacob, D. E., Viljoen, K. S., Grassineau, N. & Jagoutz, E. (2000). Remobilization in the cratonic lithosphere recorded in polycrystalline diamond. *Science* **289**, 1182–1185.

James, D. E., Boyd, F. R., Schutt, D., Bell, D. R. & Carlson, R. W. (2004). Xenolith constraints on seismic velocities in the upper mantle beneath southern Africa. *Geochemistry, Geophysics, Geosystems* **5**, Q01002, doi:10.1029/2003GC000551.

Katayama, I. & Nakashima, S. (2003). Hydroxyl in clinopyroxene from the deep subducted crust: Evidence for H_2O transport into the mantle. *American Mineralogist* **88**, 229–234.

Katayama, I., Hirose, K., Yurimoto, H. & Nakashima, S. (2003). Water solubility in majoritic garnet in subducting oceanic crust. *Geophysical Research Letters* **30**, 2155, doi:10.1029/2003GL018127.

Kelemen, P. B., Hart, S. R. & Bernstein, S. (1998). Silica enrichment in the continental upper mantle via melt/rock reaction. *Earth and Planetary Science Letters* **164**, 387–406.

Kerrick, D. M. & Connolly, J. A. D. (2001). Metamorphic devolatilization of subducted marine sediments and the transport of volatiles into the Earth's mantle. *Nature* **411**, 293–296.

Kessel, R., Schmidt, M. W., Pettke, T. & Ulmer, P. (2005*a*). Fluid and melt compositions coexisting with eclogite at high pressure and temperature. *Geochimica et Cosmochimica Acta* **69**, A658–A658.

Kessel, R., Ulmer, P., Pettke, T., Schmidt, M. W. & Thompson, A. B. (2005*b*). The water–basalt system at 4 to 6 GPa: Phase relations and second critical endpoint in a K-free eclogite at 700 to 1400°C. *Earth and Planetary Science Letters* **237**, 873–892.

Klein-BenDavid, O., Izraeli, E. S., Hauri, E. & Navon, O. (2007). Fluid inclusions in diamonds from the Diavik mine, Canada and the evolution of diamond-forming fluids. *Geochimica et Cosmochimica Acta* **71**, 723–744.

Krogh, E. J. (1988). The garnet–clinopyroxene Fe–Mg geothermometer—a reinterpretation of existing experimental data. *Contributions to Mineralogy and Petrology* **99**, 44–48.

Lambert, I. B. & Wyllie, P. J. (1972). Melting of gabbro (quartz eclogite) with excess water to 35 kilobars, with geological applications. *Journal of Geology* **80**, 693–708.

Laporte, D., Toplis, M. J., Seyler, M. & Devidal, J. L. (2004). A new experimental technique for extracting liquids from peridotite at very low degrees of melting: application to partial melting of depleted peridotite. *Contributions to Mineralogy and Petrology* **146**, 463–484.

Li, Z. X. A., Lee, C. T. A., Peslier, A. H., Lenardic, A. & Mackwell, S. J. (2008). Water contents in mantle xenoliths from the Colorado Plateau and vicinity: Implications for the mantle rheology and hydration-induced thinning of continental lithosphere. *Journal of Geophysical Research—Solid Earth* **113**, B09210, doi:10.1029/2007JB005540.

Litasov, K. & Ohtani, E. (2010). The solidus of carbonated eclogite in the system $CaO–Al_2O_3–MgO–SiO_2–Na_2O–CO_2$ to 32 GPa and carbonatite liquid in the deep mantle. *Earth and Planetary Science Letters* **295**, 115–126.

Litasov, K. D., Safonov, O. G. & Ohtani, E. (2010). Origin of Cl-bearing silica-rich melt inclusions in diamonds: Experimental evidence for an eclogite connection. *Geology* **38**, 1131–1134.

Macgregor, I. D. & Carter, J. L. (1970). The chemistry of clinopyroxenes and garnets of eclogite and peridotite xenoliths from the Roberts Victor mine, South Africa. *Physics of the Earth and Planetary Interiors* **3**, 391–397.

Molina, J. F. & Poli, S. (2000). Carbonate stability and fluid composition in subducted oceanic crust: an experimental study on H_2O-CO_2-bearing basalts. *Earth and Planetary Science Letters* **176**, 295–310.

Nishihara, Y., Shinmei, T. & Karato, S. (2006). Grain-growth kinetics in wadsleyite: Effects of chemical environment. *Physics of the Earth and Planetary Interiors* **154**, 30–43.

Peacock, S. M. (2003). Thermal structure and metamorphic evolution of subducting slabs. In: Eiler, J. (ed.) *Inside the Subduction Factory, Geophysical Monograph, American Geophysical Union* **138**, 7–22.

Pertermann, M. & Hirschmann, M. M. (2003). Anhydrous partial melting experiments on MORB-like eclogite: Phase relations, phase compositions and mineral–melt partitioning of major elements at 2–3 GPa. *Journal of Petrology* **44**, 2173–2201.

Peslier, A. H., Woodland, A. B., Bell, D. R. & Lazarov, M. (2010). Olivine water contents in the continental lithosphere and the longevity of cratons. *Nature* **467**, 78–81.

Poli, S., Franzolin, E., Fumagalli, P. & Crottini, A. (2009). The transport of carbon and hydrogen in subducted oceanic crust: An experimental study to 5 GPa. *Earth and Planetary Science Letters* **278**, 350–360.

Pyle, J. M. & Haggerty, S. E. (1998). Eclogites and the metasomatism of eclogites from the Jagersfontein Kimberlite: Punctuated transport and implications for alkali magmatism. *Geochimica et Cosmochimica Acta* **62**, 1207–1231.

Rapp, R. P., Shimizu, N., Norman, M. D. & Applegate, G. S. (1999). Reaction between slab-derived melts and peridotite in the mantle wedge: experimental constraints at 3·8 GPa. *Chemical Geology* **160**, 335–356.

Ritsema, J., Nyblade, A. A., Owens, T. J., Langston, C. A. & VanDecar, J. C. (1998). Upper mantle seismic velocity structure beneath Tanzania, east Africa: Implications for the stability of cratonic lithosphere. *Journal of Geophysical Research—Solid Earth* **103**, 21201–21213.

Rosenthal, A. (2010). Exploring the melting behaviour of the Earth's heterogeneous upper mantle. Research School of Earth Sciences, Australian National University, PhD thesis.

Rudnick, R. L., McDonough, W. F. & Chappell, B. W. (1993). Carbonatite metasomatism in the northern Tanzanian mantle: petrographic and geochemical characteristics. *Earth and Planetary Science Letters* **114**, 463–475.

Schulze, D. J. (1989). Constraints on the abundance of eclogite in the upper mantle. *Journal of Geophysical Research—Solid Earth and Planets* **94**, 4205–4212.

Schulze, D. J. & Helmstaedt, H. (1988). Coesite–sanidine eclogites from kimberlite—products of mantle fractionation or subduction. *Journal of Geology* **96**, 435–443.

Sekine, T. & Wyllie, P. J. (1982). The system granite–peridotite–H_2O at 30 kbar, with applications to hybridization in subduction zone magmatism. *Contributions to Mineralogy and Petrology* **81**, 190–202.

Simon, N. S. C., Carlson, R. W., Pearson, D. G. & Davies, G. R. (2007). The origin and evolution of the Kaapvaal cratonic lithospheric mantle. *Journal of Petrology* **48**, 589–625.

Spandler, C., Yaxley, G., Green, D. H. & Rosenthal, A. (2008). Phase relations and melting of anhydrous K-bearing eclogite from 1200 to 1600°C and 3 to 5 GPa. *Journal of Petrology* **49**, 771–795.

Staudigel, H. (2003). Hydrothermal alteration processes in the oceanic crust. In: Holland, H. D. & Turekian, K. K. (eds) *Treatise on Geochemistry, Volume 3*. Oxford: Elsevier Pergamon, pp. 511–535.

Stolper, E. (1982). Water in silicate glasses: An infrared spectroscopic study. *Contributions to Mineralogy and Petrology* **81**, 1–17.

Taylor, L. A. & Neal, C. R. (1989). Eclogites with oceanic crustal and mantle signatures from the Bellsbank kimberlite, South Africa, part I: mineralogy, petrography, and whole rock chemistry. *Journal of Geology* **97**, 551–567.

Taylor, W. R. & Green, D. H. (1988). Measurement of reduced peridotite–C–O–H solidus and implications for redox melting of the mantle. *Nature* **332**, 349–352.

Thomsen, T. B. & Schmidt, M. W. (2008). Melting of carbonated pelites at 2·5–5·0 GPa, silicate–carbonatite liquid immiscibility, and potassium–carbon metasomatism of the mantle. *Earth and Planetary Science Letters* **267**, 17–31.

Urakawa, S., Kondo, T., Igawa, N., Shimomura, O. & Ohno, H. (1994). Synchrotron radiation study on the high-pressure and high-temperature phase relations of $KAlSi_3O_8$. *Physics and Chemistry of Minerals* **21**, 387–391.

Veksler, I. V., Petibon, C., Jenner, G. A., Dorfman, A. M. & Dingwell, D. B. (1998). Trace element partitioning in immiscible silicate–carbonate liquid systems: An initial experimental study using a centrifuge autoclave. *Journal of Petrology* **39**, 2095–2104.

Walter, M. (1999). Melting residues of fertile peridotite and the origin of cratonic lithosphere. In: Fei, Y. W., Bertka, C. M. & Mysen, B. O. (eds) *Mantle Petrology: Field Observations and High-Pressure Experimentation (a Tribute to Francis R. (Joe) Boyd)*. Geochemical Society Special Publication **6,** 225–239.

Weiss, Y., Kessel, R., Griffin, W. L., Kiflawi, I., Klein-BenDavid, O., Bell, D. R., Harris, J. W. & Navon, O. (2009). A new model for the evolution of diamond-forming fluids: Evidence from microinclusion-bearing diamonds from Kankan, Guinea. *Lithos* **112**, 660–674.

Wilson, D., Aster, R., West, M., Ni, J., Grand, S., Gao, W., Baldridge, W. S., Semken, S. & Patel, P. (2005). Lithospheric structure of the Rio Grande rift. *Nature* **433**, 851–855.

Woodland, A. B. & Koch, M. (2003). Variation in oxygen fugacity with depth in the upper mantle beneath the Kaapvaal craton, Southern Africa. *Earth and Planetary Science Letters* **214**, 295–310.

Yagi, A., Suzuki, T. & Akaogi, M. (1994). High-pressure transitions in the system $KAlSi_3O_8$–$NaAlSi_3O_8$. *Physics and Chemistry of Minerals* **21**, 12–17.

Yasuda, A., Fujii, T. & Kurita, K. (1994). Melting phase relations of an anhydrous mid-ocean ridge basalt from 3 to 20 GPa—Implications for the behavior of subducted oceanic crust in the mantle. *Journal of Geophysical Research—Solid Earth* **99**, 9401–9414.

Yaxley, G. M. & Brey, G. P. (2004). Phase relations of carbonate-bearing eclogite assemblages from 2·5 to 5·5 GPa: implications for petrogenesis of carbonatites. *Contributions to Mineralogy and Petrology* **146**, 606–619.

Yaxley, G. M. & Green, D. H. (1994). Experimental demonstration of refractory carbonate-bearing eclogite and siliceous melt in the subduction regime. *Earth and Planetary Science Letters* **128**, 313–325.

Yaxley, G. M., Green, D. H. & Klapova, H. (1994). The refractory nature of carbonate during partial melting of eclogite: evidence from high pressure experiments and natural carbonate-bearing eclogites. *Mineralogical Magazine* **58A**, 996–997.

Zedgenizov, D. A., Ragozin, A. L., Shatsky, V. S., Araujo, D. & Griffin, W. L. (2011). Fibrous diamonds from the placers of the northeastern Siberian Platform: carbonate and silicate crystallization media. *Russian Geology and Geophysics* **52**, 1298–1309.